Journal of Catalysis 442 (2025) 115800

Contents lists available at ScienceDirect

Journal of Catalysis

journal homepage: www.elsevier.com/locate/jcat

Research article

Electronic and geometric features controlling the reactivity of Mg-vanadate and V_2O_5 surfaces toward the initial C–H activation of C_1–C_3 alkanes – A DFT+U study

Hansel Montalvo-Castro [a], Álvaro Loaiza-Orduz [b], Randall J. Meyer [c], Craig Plaisance [b], David Hibbitts [a,*]

[a] Department of Chemical Engineering, University of Florida, Gainesville, FL 32611, United States
[b] Cain Department of Chemical Engineering, Louisiana State University, Baton Rouge, LA 70803, United States
[c] ExxonMobil Technology and Engineering Company, Annandale, NJ 08801, United States

ARTICLE INFO

Keywords:
Oxidative dehydrogenation
Magnesium vanadates
Reactivity descriptors
Alkane activation

ABSTRACT

This work employs density functional theory (DFT+U) calculations to explore initial C–H activations in C_1–C_3 alkanes on V_2O_5, MgV_2O_6 (meta-vanadate), $Mg_2V_2O_7$ (pyro-vanadate), and $Mg_3V_2O_8$ (ortho-vanadate) surfaces. These materials are selective catalysts for the oxidative dehydrogenation (ODH) of alkanes into alkenes, which offers practical and thermodynamic advantages over non-oxidative alkane dehydrogenation. The geometric and electronic properties that govern the reactivity of these materials, however, have not been explored by theory despite their importance in controlling rate determining alkane initial C–H activation during ODH catalysis. In this work, we explore fourteen low-energy surfaces of $Mg_xV_2O_{x+5}$ ($x = 0$–3) exposing 64 distinct O atoms (reaction sites). C–H activation barriers are largest on $Mg_3V_2O_8$, lower and similar for $Mg_2V_2O_7$ and MgV_2O_6, and lowest for V_2O_5 surfaces; these predicted trends are consistent with measured ODH reactivity in earlier studies. Barriers are lowest (on average) when alkanes react with O atoms bound to a single V atom, with bridging O atoms having slightly higher barriers, and three-fold O atoms having the largest activation barriers. However, there is scattering within each subset indicating that factors beyond O-atom coordination have a significant role in the barriers. Vacancy formation energies (VFE) and the O 2p band energies were found to be weak descriptors of surface O reactivity for alkane activation barriers. Hydrogen addition energy (HAE) and methyl addition energy (MAE) values, in contrast, were found to correlate well with alkane activation barriers. MAE, however, outperforms HAE correlations because of the tendency of H* to form H-bonds with nearby surface O atoms, and those H-bonds are absent in C–H activation transition states causing scatter in the correlation of barriers with HAE. Constrained-orbital DFT methods were used to establish a theoretical thermochemical cycle that decouples surface reduction by CH_3* into three components: surface distortion, orbital localization, and bond formation. These results give insights into how Mg:V ratios, surface structure (O-atom coordination), and reducibility (HAE, MAE) impact the reactivity of vanadium-based metal oxides toward alkane activation.

1. Introduction

Light alkanes (C_2–C_4) are abundant in unconventional fossil resources (e.g., shale gas) and their partial oxidation to form light alkenes is desired [1,2]. Alkenes are currently produced from steam cracking, fluid-catalytic-cracking, and catalytic dehydrogenation technologies [3–6]. These processes, however, are endothermic and present significant practical challenges. For example, cracking technologies mainly produce ethylene over propylene, which is inconsistent with their current demand. Moreover, alkane dehydrogenation is endothermic and thus often limited to low-conversion, and their catalysts deactivate because of coke formation [7]. An alternative route for alkene production is the partial oxidative dehydrogenation (ODH) of alkanes, which is exothermic [1,8–13]. However, ODH reactions are also prone to low alkene selectivity because of over-oxidation pathways that form undesired CO_x products. These complete oxidation pathways hinder ODH from becoming an economically feasible contender to catalytic cracking and dehydrogenation. Whether forming the desired alkene product or

---

* Corresponding author.
E-mail address: hibbitts@che.ufl.edu (D. Hibbitts).

https://doi.org/10.1016/j.jcat.2024.115800
Received 14 October 2024; Accepted 15 October 2024

undesired CO_x products, it is thought that alkane activation is the rate determining step for alkane ODH on most catalysts of interest [14,15], and this has been explicitly shown by DFT for propane ODH on monomeric VO_x supported on silica models [16].

The kinetic selectivity during alkane ODH reaction on vanadium-oxide (VO_x) based catalysts is relatively high—relative to other metal-oxide systems—toward desired alkene products, likely governed by the extent of VO_x loading (isolation) on supports [1,17–30]. Kinetic studies on ethane and propane ODH exploring the role of VO_x density [31–40] suggest that alkene selectivities are generally higher on dispersed VO_x species than on extended V_2O_5 clusters or surfaces. At relatively low VO_x loadings on supports, isolated VO_4 species are formed, namely, monovanadates [31,41–43]. As the vanadium loading increases, the surface configuration evolves from isolated monovanadate to polymeric polyvanadates, and eventually, a vanadia monolayer surface coverage is reached. In general, isolated tetrahedral VO_x species are more selective but less active than polymeric VO_x and crystalline V_2O_5. For example, kinetic measurements of propane ODH on VO_x/Al_2O_3 catalysts (663 K, 14 kPa C_3H_8, 1.7 kPa O_2, balance He) show that the initial (zero conversion) propane selectivity is ~85 % at low vanadia surface density (1.4 V nm^{-2}) [31], but decreases to values ~75 % with increasing VO_x surface density (34.2 V nm^{-2}). This, in turn, suggest that spatial isolation of VO_x groups provides tunability for surface activity and selectivity during ODH reaction.

Mg-vanadate ($Mg_xV_2O_{5+x}$, x = 1–3) catalysts contain VO_4 tetrahedra within their oxide lattice and expose reactive VO_x species at their surfaces, and they have been examined for the ODH of C_2H_6 and C_3H_8 (explicitly considered in this work), as well as for larger *n*-alkanes (C_4–C_8) and cyclohexane [1,10,12,21,29,31,38,41,44–54]. Alkene selectivities are generally higher for ortho-vanadate ($Mg_3V_2O_8$) than for pyro-vanadate ($Mg_2V_2O_7$) or meta-vanadate (MgV_2O_6) structures, and this has been attributed to the geometric arrangement of VO_4 tetrahedra within their bulk structures. For example, during the ODH of butane on Mg-vanadate surfaces (813 K, butane/O_2/He = 4:8:88) the total selectivity toward butene and butadiene was 56.0 % for $Mg_3V_2O_8$, while being only 14 and 16 % for MgV_2O_6 and $Mg_2V_2O_7$, respectively [55]. As the Mg:V ratio increases, VO_4 tetrahedra go from forming edge-sharing chains (in MgV_2O_6) to corner-sharing dimers (in $Mg_2V_2O_7$) to being completely isolated from each other (in $Mg_3V_2O_8$). This suggests, consistent with the work on supported VO_x complexes [31–40], that dispersed VO_4 tetrahedra lead to higher alkene selectivities than dimers or extended complexes. This series of metal vanadates ($M_xV_2O_{5+x}$, x = 1–3) offers the ability to modify VO_x-spacing within a crystal lattice by changing M:V ratios without altering either oxidation state. Furthermore, these metal vanadates can be synthesized with different divalent cations as well cation mixtures to produce a larger design space of potential ODH catalysts [56–68]. Despite the high selectivities observed on Mg-vanadate catalysts, these materials have not been studied using density functional theory (DFT) calculations.

While selectivity remains the most critical feature of ODH catalysts, the initial C–H activation of alkanes is likely the rate determining step [69,70] and the surface features which govern reactivity may also influence the competing C–H bond activations to form desired alkenes and undesired CO_x products. Thus, many studies of partial ODH have focused on the initial C–H activation of alkanes [71–73]. Initial propane ODH rates (773 K, 9 kPa C_3H_8, 1.5 kPa O_2, balance N_2) were 0.072, 0.062, and 0.049 s^{-1} for MgV_2O_6, $Mg_2V_2O_7$, and $Mg_3V_2O_8$ respectively, suggesting that the reactivity on Mg-vanadates decreases with increasing Mg:V ratios [74]. This is consistent with an independent study contrasting Mg, Zn, and Pb vanadates for propane ODH that demonstrated that rates (773 K, 40 vol% C_3H_8, 20 vol% O_2/N_2) normalized by surface area were approximately 10-times higher for catalysts containing a mixture of V_2O_5 and MgV_2O_6 than for either pure $Mg_2V_2O_7$ or $Mg_3V_2O_8$ catalysts [75]. These observations on initial propane ODH rates are also consistent with H_2 temperature programed reduction experiments that demonstrate earlier reduction temperature onsets on Mg-vanadates of lower Mg:V ratio [76], as well as with electrical conductivity *in situ* measurements during propane ODH that suggest faster consumption rates on MgV_2O_6 and $Mg_2V_2O_7$ relative to $Mg_3V_2O_8$ [77]. These results, and the selectivity results described earlier, suggest that isolating VO_x species within the metal-vanadate lattice decreases alkane activation rates and increases alkene selectivity.

While no DFT studies exist for Mg-vanadate catalysts, many calculations have examined alkane activations on oxides as motivated by ODH and other partial oxidations, such as the oxidative coupling of methane [78–81]. Scaling relationships for C–H activation in alkanes (C_1–C_4) and alkanols (C_1–C_3) were developed on a series of POM clusters ($H_3PMo_{12}O_{40}$, $H_4SiMo_{12}O_{40}$, H_3PW_{12} O_{40}, $H_4PVMo_{11}O_{40}$, and $H_4PVW_{11}O_{40}$) [82]. Using DFT+U (U = 6.0–8.0 eV) calculations, it was found that the reactivity of surface oxygens could be described using their hydrogen addition energy (HAE, the energy to add a H atom to a surface O atom to form hydroxyl) and that activation barriers could be predicted with a combination of HAE values and the bond dissociation energy of the C–H bond in the reacting alkane or alkanol. HAE, furthermore, has been shown to be a suitable descriptor for C–H activation on MoVTeNbO(001) [83], doped-Co_3O_4 [84], and NiO [85] catalysts. DFT calculations contrasting the reactivity of VO_2^+, $V_3O_7^+$, V_4O_{10}, and $O = V(O^-)_3$ cluster models for propane and but-1-ene ODH also report that the corresponding C–H activation energies on these systems correlate with their HAE [86].

Vacancy formation energies (VFE) have also been previously used as a descriptor for C–H activation of alkanes. For example, density functional theory (DFT + U) calculations on CeO_2 surfaces found that the energy for the dissociative adsorption of methane (*H and *CH_3) correlates with the corresponding oxygen vacancy formation energies [87]. Such correlation was also shown across doped CeO_2 surfaces with a substitutional dopant M (28 M dopants were examined) [81,87–91], suggesting that VFE is a ubiquitous descriptor for C–H activation of CH_4 on Ce-based oxides. DFT calculations on rutile TiO_2 (110) surface doped with V, W, Cr, Mo, and Mn also demonstrate that VFE values well-correlate with CO oxidation reaction energies and O_2 adsorption (onto a vacancy) energies [92]. This work is consistent with prior studies that qualitatively related ODH reaction rates to surface oxide reducibility [30,43,93–96]. VFE and HAE values have been also employed to discriminate the relative reactivity among VO_x clusters on various supports, (e.g., Al_2O_3, SiO_2, and CeO_2) [97–100] although not shown to explicitly correlate with alkane initial C–H activation in these works.

Chemical descriptors such as HAE and VFE have also been explored on perovskite-type catalysts. For example, DFT calculations across a large subset of perovskites with ABO_3 stoichiometry found that both, VFE and HAE values well correlate with homolytic C–H activation energies in CH_4 with mean absolute errors of <0.2 eV [101]. In addition to chemical descriptors, machine learning approaches have been pursued in combination with experimental measurements to explore property-function relationships during ethane, propane, and n-butane oxidation on V and Mn-based oxides [102]. Overall, reactivity descriptors are desired for the prediction of activity, yet they also inform about the surface properties that govern the reactivity of metal-oxide catalysts and thus may give insights into ODH selectivities.

Here, we employ DFT+U and constrained-orbital (co-DFT) calculations to produce a systematic study of the reactivity of Mg-vanadates ($Mg_xV_2O_{5+x}$, x = 1–3) and vanadia (V_2O_5) toward the initial C–H activation of C_1–C_3 alkanes. For pyrovanadate ($Mg_2V_2O_7$), both the triclinic and monoclinic phases were examined as both can be synthesized [77]. For each material examined, we calculated surface formation energies (SFE) for multiple terminations of low-index surface slabs and then evaluated initial C–H activation reactions on fourteen distinct low-energy surfaces, exposing 64 distinct reaction sites (O atoms). Alkane activation barriers were lowest on V_2O_5, followed by VO_4-corner-sharing $Mg_2V_2O_7$, VO_4-edge-sharing MgV_2O_6, and isolated-VO_4 $Mg_3V_2O_8$ showing the highest barriers, in direct agreement with prior reports. V=O were found to be slightly more reactive (on average) than bridging O atoms, while three-fold O atoms were significantly less reactive. Among the different alkanes, activation barriers trend with BDE values of the C–H bonds of interest, as expected. VFE, HAE, and methyl addition energies (MAE) correlate with alkane activation barriers, as previously reported for VFE and HAE. Among these, MAE correlates best, and structural data suggests that MAE outperformed the commonly used HAE because adsorbed H* atoms used in HAE calculations often formed H-bonds with adjacent surface O atoms that were not representative of H-atom geometries in alkane activation transition states, thus worsening HAE-based predictions. These insights into surface reactivity patterns were further bolstered by constrained orbital DFT calculations that deconvolute MAE values into a thermochemical cycle that includes surface distortion (geometry) and electron localization energies. Overall, this work elucidates the geometric and electronic features of Mg-vanadate catalysts that govern their reactivity during alkane ODH, extends prior knowledge of alkane reactivity descriptors on oxides, and establishes the groundwork for ongoing studies of alkane ODH selectivity and the behavior of doped Mg-vanadate materials.

2. Methods

Periodic density functional theory (DFT) calculations were performed using the Vienna ab initio simulation package (VASP) [103–106] and implemented in the Computational Catalysis Interface [107]. Planewave basis sets were constructed with the projector augmented wave (PAW) potentials with an energy cutoff of 396 eV. The exchange and correlation energies were estimated with the Perdew-Burke-Ernzerhof (PBE) form of the generalized gradient approximation (GGA) [108,109].

Gas calculations were performed in a 15 Å × 15 Å × 15 Å vacuum unit cell. Atomic positions were optimized until the maximum force on all atoms was <0.05 eV $Å^{-1}$. Gas phase calculations for O_2 were performed spin-polarized to account for its triplet state. Previous DFT calculations exploring the electrochemical oxygen reduction and evolution reactions have shown that PBE-calculated O_2 energies are underestimated (too exothermic) based on H_2O formation free energies [110,111]. As such, a semiempirical correction of +0.46 eV was applied to O_2 gas-phase energies as calculated by PBE.

The GGA approach, however, often results in strong-self interactions that raise from the exchange–correlation error in 3*d* orbitals (present in V). This has been shown to systematically penalize reduced states over oxidized states (i.e., with more *d* electrons) across multiple transition metal oxides [112], resulting in an overall overestimation of oxidation energies. Therefore, we implemented the DFT+U approach,[113–115] which introduces an on-site Coulombic interaction (the *U*-term) that penalizes partial occupation of localized orbitals and thus electron delocalization. Here, we use a $U = 3.0$ eV for V atoms, which is consistent with previous DFT studies on vanadium oxides that reproduce experimentally verifiable properties [112,116–124]. For example, the band gap of V_2O_5, experimentally measured to be 2.0 eV, was reproduced by DFT when using a *U*-value of 3.1 eV, compared to the GGA method only (which predicted a band gap of 1.6 eV) [112].

The unit cell bulk structures for vanadium pentoxide (V_2O_5), metavanadate (MgV_2O_6), pyrovanadate ($Mg_2V_2O_7$), and orthovanadate ($Mg_3V_2O_8$) were built from crystallographic data and then both the atomic coordinates and lattice parameters were optimized using DFT+U. A set of three *k*-point meshes was systematically tested during bulk optimizations (Fig. S1) to guarantee that the converged DFT energy value was not sensitive to *k*-point selection (within 10^{-2} eV). The *k*-point meshes ranged from 2 × 5 × 6 to 4 × 11 × 13 for V_2O_5, 3 × 8 × 4 to 9 × 24 × 12 for MgV_2O_6, 2 × 5 × 6 to 6 × 16 × 18 for tri-$Mg_2V_2O_7$, 4 × 3 × 3 to 16x12x12 for mono-$Mg_2V_2O_7$, and 4 × 2 × 3 to 8 × 4 × 6 for $Mg_3V_2O_8$. Bulk structures were electronically converged so that energies varied by $< 10^{-6}$ eV between iterations and the maximum force on each atom was <0.05 eV Å. The lattice parameters were relaxed during optimization. The optimized bulk lattice parameters for V_2O_5 and Mg-vanadates are summarized in Table 1. The optimized bulk lattice parameters for the V_2O_5 (a = 11.62 Å, b = 4.01 Å, c = 3.58 Å) are in close agreement with those reported experimentally [125–128] as well as from previous DFT calculations [129–132] The optimized bulk parameters (Table 1) for MgV_2O_6, tri-$Mg_2V_2O_7$, mono-$Mg_2V_2O_7$, and $Mg_3V_2O_8$ also agree with those reported from experiments and calculations [77,133–140]. After optimization, the unit cell volume varied by <5 % of the experimentally measured values.

Surfaces were cut from the corresponding optimized bulk structures and further optimized using a two-step procedure, which is more efficient than conventional single-step optimizations. In the first step, structures were electronically converged so that energies varied by $<10^{-4}$ eV between iterations and the maximum force on each atom was <0.05 eV $Å^{-1}$. In the second step, structures were electronically converged so that energies varied by $<10^{-6}$ eV (more accurate) between iterations and the maximum force on each atom was <0.05 eV $Å^{-1}$. Forces for the first and second steps were computed using a fast Fourier transform grid with cutoffs of 1.5-times and 2.0-times of the planewave cutoff, respectively. All surfaces were systematically cleaved to explore multiple terminations (Table S1). The *k*-point mesh was fixed when exploring multiple terminations for a given surface, according to their corresponding cell parameters. Once the best termination per surface was found, a *k*-point mesh screening was performed to explore whether the converged optimized surface energy was not significantly changing with increasing the size of the mesh (Fig. S1).

The slab-models were generated from cleaving the bulk structure from the highest *k*-point mesh bulk calculation. Slab-models in this work are at least 3-layers thick, resulting in a range of 54–126 total number of atoms per surface. All surfaces were initially optimized with all atoms

Table 1
Experimental (exp) and calculated cell parameters of V_2O_5 and $Mg_xV_2O_{5+x}$ before (pre-opt) and after (opt) optimization.

Bulk		a/Å	b/Å	c/Å	α/deg	β/deg	γ/deg	Vol. $Å^3$ V^{-1}
V_2O_5	exp	11.51	4.37	3.56	90.00	90.00	90.00	44.77
	pre-opt	11.54	4.38	3.57	90.00	90.00	90.00	45.11
	opt	11.62	4.01	3.58	90.00	90.00	90.00	42.57
MgV_2O_6	exp	9.28	3.50	6.73	90.00	111.76	90.00	20.26
	pre-opt	9.20	3.46	6.62	90.00	113.50	90.00	20.01
	opt	9.21	3.51	6.58	90.00	114.26	90.00	21.82
m-$Mg_2V_2O_7$	exp	6.59	8.41	9.47	90.00	100.61	90.00	12.08
	pre-opt	6.60	8.41	9.47	90.00	100.61	90.00	11.81
	opt	6.57	8.35	9.40	90.00	100.35	90.00	11.58
t-$Mg_2V_2O_7$	exp	13.78	5.41	4.91	81.42	100.61	130.33	68.52
	pre-opt	13.77	5.41	4.91	81.42	106.82	130.33	66.64
	opt	13.38	5.33	4.94	81.29	106.06	130.35	64.46
$Mg_3V_2O_8$	exp	6.05	11.44	8.33	90.00	90.00	90.00	72.07
	pre-opt	6.08	11.47	8.34	90.00	90.00	90.00	72.70
	opt	6.00	11.41	8.26	90.00	90.00	90.00	70.77

relaxed within a singular unit cell. Following singular unit-cell optimizations, supercells were generated for those slabs that were not large enough to accommodate adsorbates species without introducing artefacts associated with self-interactions through periodic boundaries. During supercell optimizations, atoms from the bottom half of the slab were frozen to minimize slab reconstruction upon the addition of adsorbate species. To the best of our knowledge, there are no previous DFT investigations on Mg-vanadate surfaces, and their experimental characterization is limited to a few studies [74,140–144], therefore, a wide range of crystallographically unique Miller index cuts was systematically explored to identify the lowest surface formation energy (SFE) planes for each bulk. In this initial surface screening, the five surfaces with the lowest V-normalized SFE values were chosen for further screening. This resulted in a reduced list of 5 Miller index cuts per bulk, for a total of 25 distinct surfaces. For each of these Miller index cuts, all potential terminations that resulted in stoichiometric slabs (i.e., with a Mg:V:O ratios matching that in the bulk) were further explored. Accounting for all terminations within those 25 Miller index cuts resulted on 127 unique terminations which then were further screened based on their corresponding SFE values (Table S1).

Surface formation energies were estimated from:

$$SFE = \frac{E_{surf} - n^{*}E_{bulk}}{2^{*}A_{surf}} \quad (1)$$

where E_{surf} is the energy of the optimized surface slab model, E_{bulk} is the energy of the optimized bulk model, $2^{*}A_{surf}$ is the total surface area of the slab, and n is a stoichiometric factor between the surface model and its corresponding bulk structure. Based on SFE values, only 14 (out of 127) terminations were chosen to explore the reactivity of every unique surface oxygen atom present, resulting in 64 unique surface O reaction sites (Table S2).

For each of these unique surface O reaction sites, we performed adsorbate calculations for H* and CH_3* species as well as for reactants and products. For each oxygen, a vacancy formation calculation (O_{vac}) was performed by removing the O-atom of interest and optimizing the structure following a two-step procedure similar to those used in surface optimization calculations. Transition state searches for alkane C–H activation of C_1–C_3 alkanes were initiated using the nudge elastic band (NEB) method [145–147], with 16 images along the reaction coordinate. NEBs were converged so that the maximum force across all atoms—in all images—was <0.5 eV Å^{-1} (a much higher force than that used for structural optimizations). Following NEB convergence, transition state structures were isolated using the Dimer method [148] and optimized until the maximum force in all atoms was <0.05 eV Å^{-1} using a two-step procedure analogous to that described for optimizations. All barriers in this work are referenced to the corresponding gas-phase alkane and bare surface unless stated otherwise.

All calculations were run spin-polarized to accommodate unpaired electrons in V-atoms, consistent with previous works on V_2O_5 [16,99,100,149]. In this work, the addition of H*, CH_3*, and C_1–C_3 alkane C–H activations are single-electron reduction processes in V-atoms, as confirmed by population matrices (provided by DFT+U) that corroborate transition from closed single shell (V^{V}) to doublet (V^{IV}) electronic state. For the case of bare surfaces, we used population matrices to confirm closed single shell state on all V-atoms and discarded all bare surface models across all bulks that resulted on unpaired electrons.

Constrained-orbital DFT (co-DFT) calculations were used to deconvolute the electronic transformation underlying chemical processes (i.e., methyl-adsorption) occurring across Mg-vanadate and vanadia surfaces. This technique was developed by Plaisance *et al.* [150] and allows one to perform fully self-consistent Kohn-Sham DFT calculations in the presence of certain constraints on the form and occupancy of one or more orbitals. This method should not be confused with the fundamentally different *constrained density functional theory* (CDFT),[151] which allows only constraints on the electron density. For example, one can use co-DFT to force a single half-filled orbital to localize on a single oxygen atom. Further details on co-DFT are discussed in Section 3.4.

3. Results and discussion

3.1. Surface cleavage and formation energies

A systematic screening for many surface terminations was performed across low Miller facets, for each bulk (Table S1). Surfaces were initially optimized in a singular (1 × 1) surface unit cell. SFE values, in general, were found to be lower for surface terminations that preserve VO_4 coordination from the bulk. From these data, the lowest five formation energy surfaces were kept for further screening. This resulted in a corresponding five distinct Miller indexes per bulk, for a total of 25 distinct surfaces (Table S2).

Each of these surfaces was then systematically explored to account for all potential terminations (Table S2). Slab models that were too small to accommodate propane were reoptimized as supercells. Surface formation energy (SFE) values were used to identify the best termination for each Miller index. For the (1 0 0) surface of tri-$Mg_2V_2O_7$, two terminations had similar SFE, namely, a Mg- and a V-rich surfaces, and both were used in additional calculations. DFT+U calculations on V_2O_5 surfaces have shown that the use of supercells may result on significant restructuring that can yield relatively lower surface formation energies; [116] therefore, we report SFE values for supercells in Fig. 1. In addition to SFE calculations, the electronic structure of these surfaces was also considered to filter out unstable catalyst models. The DFT+U method reports population matrices describing orbital occupancies for each element on which the DFT+U model was used (here, for V cations). These matrices were used to obtain the formal oxidation state of lattice V-atoms. Surfaces that exhibited reduced V-atoms (indicating charge transfer between the top and bottom surfaces of these stoichiometric slabs) were excluded from further consideration.

The lowest SFE surface for V_2O_5 was found to be the (010) surface, which has traditionally been subject of both experimental [152–157] and computational [129,132,158,159] studies. The corresponding lowest SFE surfaces were found to be (001) for MgV_2O_6, (210) for t-$Mg_2V_2O_7$, (001) for m-$Mg_2V_2O_7$, and (110) for $Mg_3V_2O_3$. For each bulk, 2–3 low-index surfaces were considered further based on relative SFE values (Fig. 2 and Fig. S2). These surfaces expose a set of 64 lattice oxygen atoms (highlighted in Fig. 2) that vary in O-atom coordination (atop, bridge, and three-fold) and environment (e.g., in V–O–V and V–O–Mg bridges). The inherent differences among the oxygen surface atoms will result in distinct chemical behavior and here we explore the initial C–H activation in C_1–C_3 alkanes across all 64 oxygen atoms to identify surface features that govern reactivity in Mg-vanadate catalysts.

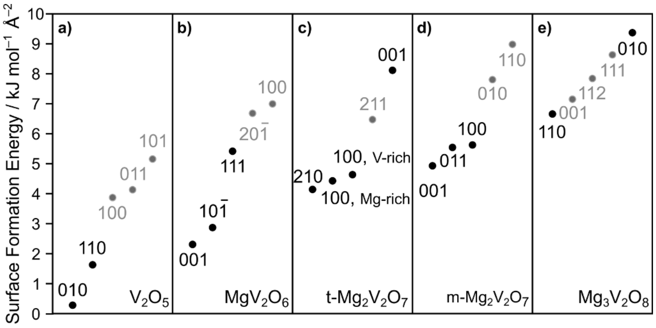

Fig. 1. Surface formation energies (SFE, kJ mol^{-1} Å^{-2}) for a) V_2O_5 (vanadium pentoxide, orthorhombic), b) MgV_2O_6 (meta-vanadate, monoclinic), c) $Mg_2V_2O_7$ (pyro-vanadate, triclinic), d) $Mg_2V_2O_7$ (pyro-vanadate, monoclinic), and e) $Mg_3V_2O_8$ (ortho-vanadate, orthorhombic) surfaces considered in this work.

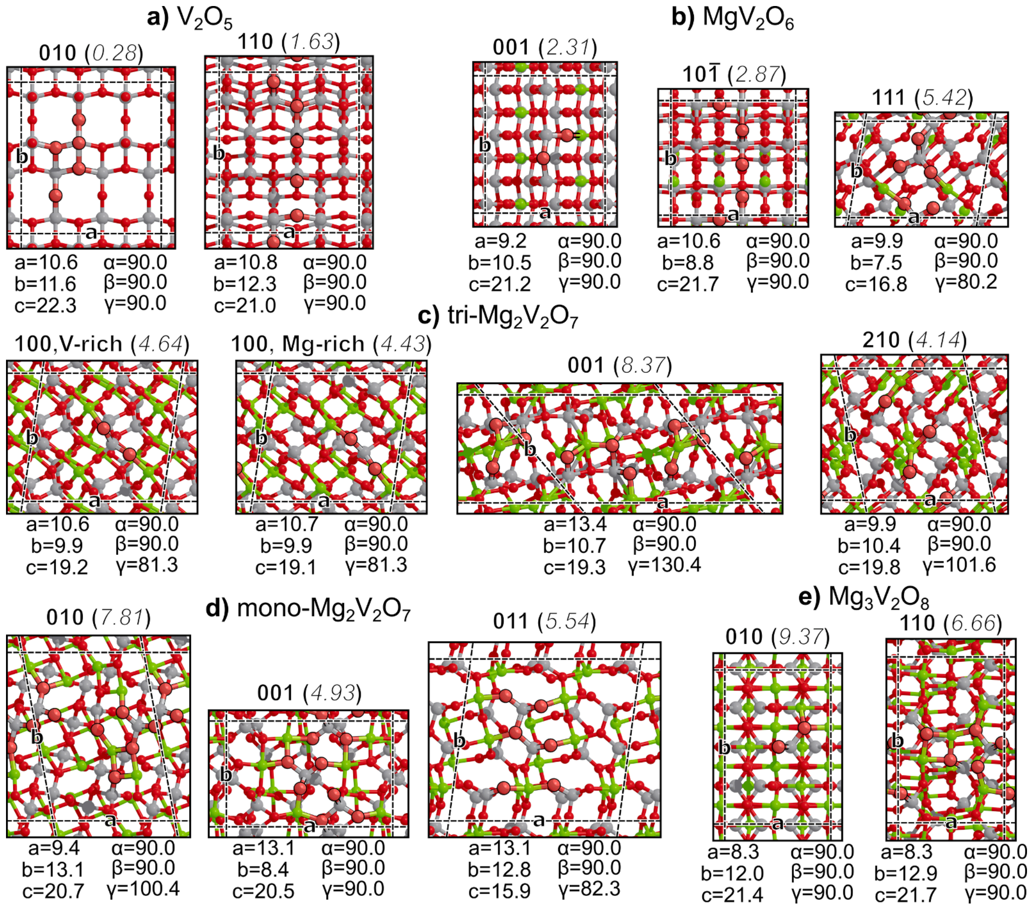

Fig. 2. Top-views of slab-structure models of a) V_2O_5 (vanadium pentoxide, orthorhombic), b) MgV_2O_6 (meta-vanadate, monoclinic), c) $Mg_2V_2O_7$ (pyro-vanadate, triclinic), d) $Mg_2V_2O_7$ (pyro-vanadate, monoclinic), and e) $Mg_3V_2O_8$ (ortho-vanadate, orthorhombic). The optimized cell parameters along with their Miller index are also provided, along with the corresponding surface formation energy value (*italics*).

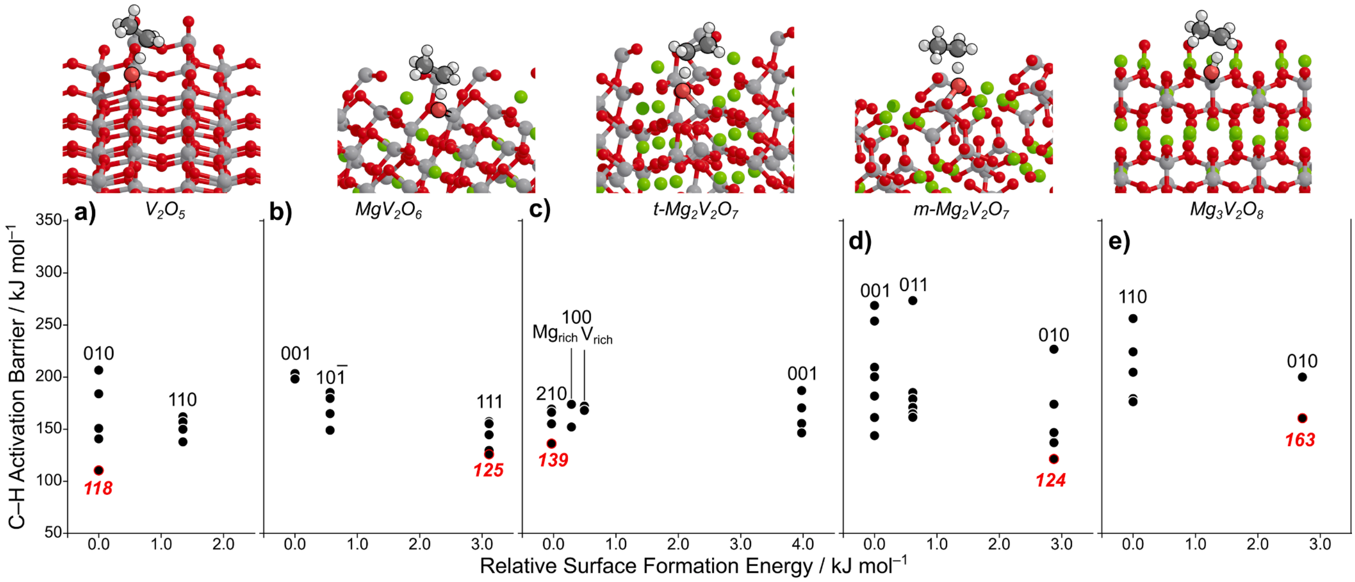

Fig. 3. Initial C–H activation energy for C_2H_6 as a function of relative surface formation energies (SFE) across the selected surfaces for a) V_2O_5, b) MgV_2O_6, c) triclinic $Mg_2V_2O_7$, d) monoclinic $Mg_2V_2O_7$, and e) $Mg_3V_2O_8$. Lattice planes are labeled by surface Miller index. Each data point corresponds to a unique O lattice atom. Values in red indicate the lowest C–H activation barrier for each bulk, irrespective of surface. Two distinct terminations (Mg-rich and V-rich) are shown for t-$M_2V_2O_7$ (1 0 0) surface. The transition state structures corresponding to the lowest C–H barrier per bulk, are also provided. Figures S3–S5 in the SI show the corresponding barriers for CH_4, α-C_3H_8, and β-C_3H_8, respectively. (For interpretation of the references to colour in this figure legend, the reader is referred to the web version of this article.)

3.2. Effect of Mg:V ratio on alkane activation energies

Initial C–H activation barriers were calculated for methane (CH_4), ethane (C_2H_6) and propane (C_3H_8). For the case of C_3H_8, the C–H activations for both the terminal (α) and central (β) positions were calculated. All activation barriers reported in this work are referenced to the corresponding bare surface and the gas-phase alkane. These are presented without van der Waals corrections which would be expected to decrease activation barriers (relative to gas precursors) for all three alkanes, with the largest impact occurring for propane activation. Initial C–H activation barriers were attempted for two distinct reaction coordinates, namely, (1) a concerted C–H activation that results in the concurrent formation of a hydroxyl (H*) and an alkyl ($C_xH_{2x–1}$*) surface species and (2) a sequential C–H activation that results in a $C_xH_{2x–1}\bullet$ radical intermediate that then becomes a surface bound alkyl. All transition states from both initial guesses converged to a radical-forming C–H activation (examples in Fig. 3), resembling a homolytic C–H activation. These transition states have average C–H bond distances near 1.6 Å, O–H bond distances near 1.1 Å, and C–H–O angles near 170 degrees. The subsequent formation of the surface-bound alkyl was found to occur with negligible barriers relative to the C–H activation barriers.

Ethane activation barriers (Fig. 3, Figs. S3–S5 in the SI for methane and propane) show that different active sites on the same surface can have very different C–H activation barriers. For example, five distinct sites (oxygen atoms) on V_2O_5 (010) lead to activation barriers ranging from 118 to 214 kJ mol^{-1}. The spread of activation energies across different reaction sites (oxygen atoms) for a given surface indicates that oxygen-specific properties govern rates rather than surface-specific properties (e.g., SFE). In considering only the most reactive O atoms for each catalyst composition, activation barriers generally increase with Mg content from 118 kJ mol^{-1} on V_2O_5 (010) to 163 kJ mol^{-1} on $Mg_3V_2O_8$ (010). These trends are also observed for methane and propane activation (Figs. S3–S5 in the SI). These reactivity trends are qualitatively consistent with experimental observations from propane ODH (793 K, 9.12 kPa C_3H_8, 1.52 kPa O_2, balance N_2) [74] that suggests that MgV_2O_6 is more reactive than $Mg_3V_2O_8$. Specifically, initial propane ODH rates on MgV_2O_6, $Mg_2V_2O_7$, and $Mg_3V_2O_8$ catalysts were 0.072 s^{-1}, 0.062 s^{-1}, and 0.049 s^{-1}, respectively, shown to be consistent with their corresponding initial reduction rates in H_2. Assuming first order kinetics on C_3H_8, the corresponding apparent activation enthalpies (ΔH_{rxn}) were reported, respectively, as 64.1 (MgV_2O_6), 89.7 ($Mg_2V_2O_7$), and 98.6 ($Mg_2V_2O_8$) kJ mol^{-1}, which consistently trend with the electronic DFT+U computed barriers (Fig. S5, 107, 123, and 145 kJ mol^{-1}) on these systems. As the Mg:V ratio increases, VO_4 tetrahedra go from forming edge-sharing chains (in MgV_2O_6) to corner-sharing dimers (in $Mg_2V_2O_7$) to being completely isolated from each other (in $Mg_3V_2O_8$). This is thought to weaken the reactivity of surface oxygen atoms[44,55] and this is corroborated by our calculations. Overall, these trends are also consistent with previous DFT calculations for propane ODH on VO_x species supported on silica, where dimers mediate C–H activations with lower free energy barriers (114 kJ mol^{-1}, 750 K) than isolated monomers (124 kJ mol^{-1}) [149].

Fig. 4 shows initial C–H activation barriers for C_2H_6 as a function of oxygen coordination and neighbors. For all surfaces examined, the most reactive O atom is either in an atop or bridge position, although many of those bridging O atoms are in V–O–Mg coordinations rather than V–O–V as increasing Mg content isolates VO_4 tetrahedra. On average, O atoms appear to be more reactive if they have fewer cation neighbors, as barriers for atop O (V═O groups, average barrier 157 kJ mol^{-1}) are lower than that for bridging O atoms (165 and 172 kJ mol^{-1} average barrier for V–O–V and V–O–Mg, respectively), which are lower than that for three-fold O atoms (>181 kJ mol^{-1} averages) as shown in Fig. 4b. Within each group, however, there is significant spread indicating that the oxygen coordination does not fully inform of their reactivity; surfaces exist where atop V are less reactive than their bridging counterparts. For bridging O sites and three-fold O sites, barriers generally increase with increasing Mg:V ratio. For example, averages values for bridged O atoms are 165 and 172 kJ mol^{-1} for V–O–V and V–O–Mg, respectively. This effect is more pronounced for three-fold coordinations, for which the corresponding average value for three-fold O atoms with three V neighbors is 181 kJ mol^{-1}, while being > 200 kJ mol^{-1} for three-fold O atoms with neighboring Mg. These conclusions are extendible to the initial C–H activation of methane and propane (Figs. S6–S8 in the SI) with barriers for each also depending on their respective BDE values as described further below.

These results across different Mg-vanadate surfaces suggest that increasing the Mg:V ratio, leading to greater VO_x isolation, increases alkane activation barriers which occur by homolytic C–H activation to reduce atop or bridging O atoms. While our calculations reflect surface properties, they are consistent with bulk measurements on Mg-vanadate systems that show larger UV–vis edge energy (reducibility proxy) values with increasing Mg:V ratios (2.3 eV in V_2O_5, 2.7 eV in MgV_2O_6, 3.4 eV in $Mg_2V_2O_7$, and 3.5 eV in $Mg_3V_2O_8$) [160]. Overall, one can infer that $Mg_3V_2O_8$ is less reactive because of the greater isolation of its VO_x compared to the other materials of interest. How these results, about initial C–H activation, directly influence selectivity is, at present, still unclear. It is likely, however, that the properties which govern alkane reactivity will also be responsible for the subsequent C–H activations to

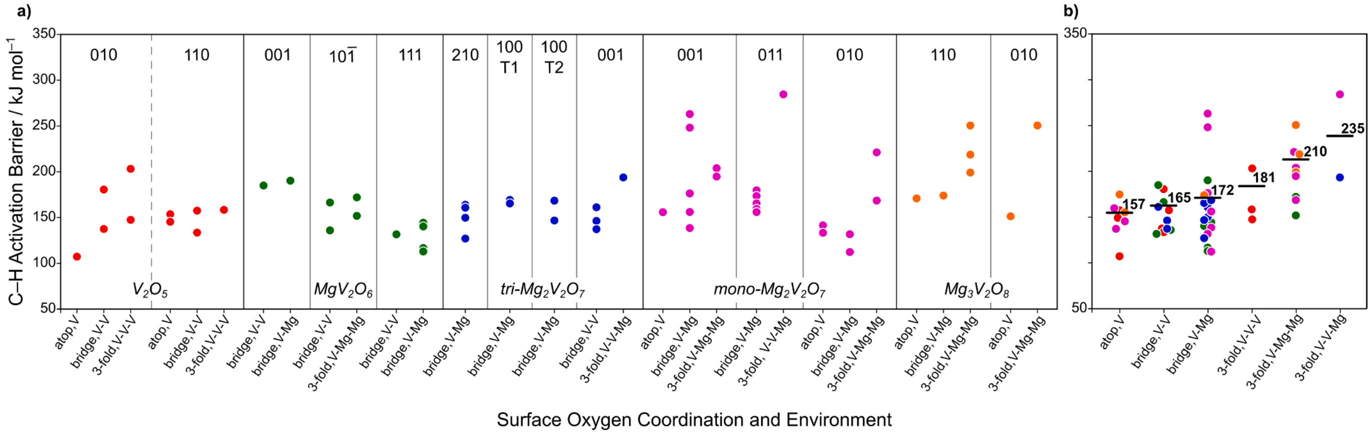

Fig. 4. Initial C–H activation energy for C_2H_6 as a function of surface oxygen coordination and environment classified a) per bulk and b) per coordination across all the selected surfaces for V_2O_5 (red), b) MgV_2O_6 (green), triclinic $Mg_2V_2O_7$ (blue) d) monoclinic $Mg_2V_2O_7$ (pink), and $Mg_3V_2O_8$ (orange). Lattice planes are labeled by surface Miller index. Each data point corresponds to a unique O lattice atom. Average values per type are also provided in panel (b). Figures S6–S8 (SI) show the corresponding barriers for CH_4, α-C_3H_8, and β-C_3H_8, respectively. (For interpretation of the references to colour in this figure legend, the reader is referred to the web version of this article.)

form the desired alkene or the undesired CO_x products. Next, we consider chemical and electronic descriptors to gain insights into those governing properties.

3.3. Catalyst properties governing C–H activation in alkanes

Section 3.2 demonstrated how increasing Mg content, with greater isolation of VO_4 tetrahedrons in the crystal, leads to higher alkane activation barriers, and that low-coordinated O atoms (atop and bridge) are more reactive than their high-coordinated (three-fold) counterparts. Here, we calculate oxygen vacancy formation energy (VFE), hydrogen addition energy (HAE), and methyl addition energy (MAE) to explore how these give insights into alkane activation barriers. All three probe the surface ability to be reduced either through O removal or reduction (to form O–H or O–CH_3 bonds).

Oxygen vacancy formation energies were calculated as the reaction energy for:

$$MO_x \rightarrow MO_{x-1} + 1/2\ O_2(g) \tag{2}$$

which gives an indication of the strength of surface-oxygen bonds. ODH proceeds via Mars van Krevelen mechanism in which the surface oxygen atoms are reduced to form H_2O and then oxygen vacancies that are subsequently healed by gas-phase O_2. As such, vacancy formation energies have been traditionally used to assess surface reducibility and thus catalytic activity.[81,87–91,116] Vacancy formation energies vary across the unique oxygen atoms for a given surface, as shown in Fig. 5. For example, VFE values for V_2O_5 (010) range from 153–369 kJ mol^{-1}. Surfaces with higher SFE values are expected to be more reactive, and this is generally consistent with their corresponding VFE values. Considering the most facile oxygens to deplete (red in Fig. 5), a weak correlation exists with Mg-content; increasing Mg:V ratios increase VFE values. This is consistent with prior experimental studies of the reducibility of Mg-vanadates,[76,77] showing that the orthovanadate ($Mg_3V_2O_8$) is less reducible than the metavanadate (MgV_2O_6).

The VFE values along with their corresponding initial C–H activation barriers for C_1–C_3 alkanes are shown in Fig. 6. While there is a qualitative trend between the C–H activation barriers of C_1–C_3 alkanes with their corresponding oxygen VFE values, there is also significant scatter. This is likely because the structural and electronic changes associated with forming an oxygen vacancy in these systems are severe when compared to those present upon forming a C–H activation transition state. As such, it is likely that VFE descriptors are limited to materials that are resistant to surface restructuring upon surface O vacancy formation, as it is the case of perovskite materials [101]. DFT estimated VFE values have also been shown to correlate with experimentally measured effective activation energies for CH_4 oxidation across a series of La_2O_3 doped materials (Cu, Zn, Mg, Fe, Nb, Ti, Zr, or Ta) [161]. The VFE values for these La_2O_3 doped surfaces, however, fell along two distinct correlations, suggesting that barriers are weakly sensitive to VFE for low-VFE materials (Cu, Zn, Mg, and Fe) while strongly sensitive to high-VFE materials (Nb, Ti, Zr, and Ta).

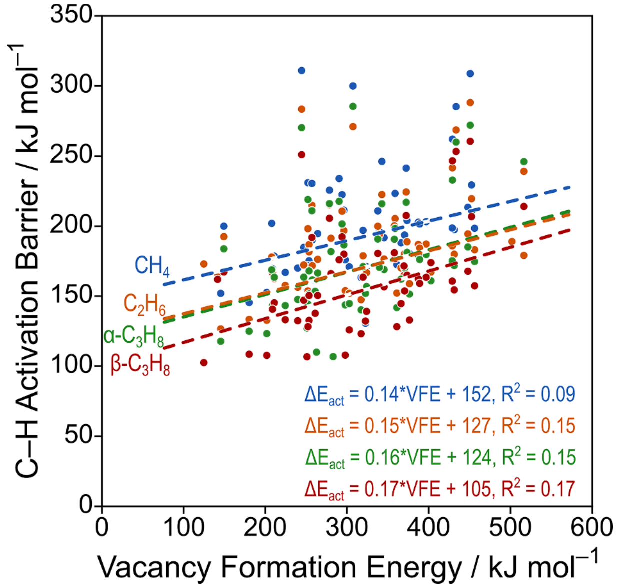

Fig. 6. Initial C–H activation barrier of methane (CH_4; blue), ethane (C_2H_6; orange), and propane (a-C_3H_8; green; b-C_3H_8; red) as a function of the oxygen vacancy formation energies (VFE) across selected surfaces for V_2O_5, MgV_2O_6, tri- and mono-$Mg_2V_2O_7$, and $Mg_3V_2O_8$ bulks. Each data point corresponds to a unique surface oxygen atom. Electronic barriers (kJ/mol) are reported relative to the corresponding bare surface and gas phase alkane. Linear regressions with their corresponding R^2 values are also provided. (For interpretation of the references to colour in this figure legend, the reader is referred to the web version of this article.)

Hydrogen addition energies were calculated as the reaction energy for:

$$MO + 1/2\ H_2O\ (g) \rightarrow MO-H + 1/4\ O_2(g) \tag{3}$$

where gaseous H_2O and O_2 are used here to balance the H addition rather than alternatives (H radicals or ½ H_2 (g)) that are not present during ODH reactions. While the strength of the numerical correlations with HAE is independent of the chosen gas-phase reference, using H_2O and O_2 is valuable because it serves as a direct proxy to hydroxyl (MO–H) formation during ODH of alkanes, according to Eq. (3), and thus gives some indication of expected surface hydroxyl concentrations. HAE values in this work range from 17–221 kJ mol^{-1}, with average values

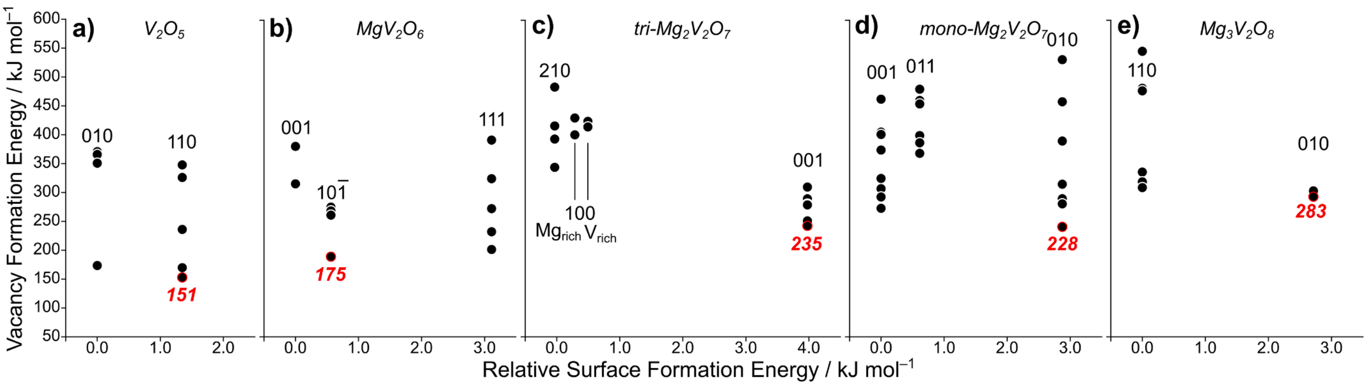

Fig. 5. Vacancy formation energies (VFE) as a function of relative surface formation energies (SFE) across examined surfaces for a) V_2O_5, b) MgV_2O_6, c) triclinic $Mg_2V_2O_7$, d) monoclinic $Mg_2V_2O_7$, and e) $Mg_3V_2O_8$. Lattice planes are labeled by surface Miller index. Each data point corresponds to a vacancy from unique O lattice atoms.

across surfaces of 70 kJ mol^{-1} for V_2O_5, 50 kJ mol^{-1} for MgV_2O_6, 59 kJ mol^{-1} for tri-$Mg_2V_2O_6$, 93 kJ mol^{-1} for mono-$Mg_2V_2O_6$, and 117 kJ mol^{-1} for $Mg_3V_2O_8$. These HAE values indicate that MO-H formation is endothermic across V_2O_5 and Mg-vanadate surfaces. The entropy of surface-bound H* was calculated as 30 J mol^{-1} K^{-1} through harmonic oscillator analysis of the vibrational frequencies of H* on the V_2O_5 (010) surface. Taking that entropy as a constant, we can estimate that the corresponding free energies of HAE (Eq. (3) range from 37–241 kJ mol^{-1} at 773 K, and this would suggest that hydroxyl coverages would be low on these surfaces unless operating at high alkane:O_2 ratios and high conversion (leading to large H_2O:O_2 ratios).

HAE has been used to describe the reactivity of surface oxygens during C–H activation in alkanes (C_1–C_4) and alkanols (C_1–C_3) across a series of POM clusters ($H_3PMo_{12}O_{40}$, $H_4SiMo_{12}O_{40}$, $H_3PW_{12}O_{40}$, $H_4PVMo_{11}O_{40}$, and $H_4PVW_{11}O_{40}$) [82]. HAE, furthermore, has been shown to be a suitable descriptor for C–H activation over MoVTeNbO (001) [83], doped-Co_3O_4 [84], and NiO [85] catalysts. Hydrogen addition energies also vary across the unique oxygen atoms for a given surface, as for V_2O_5(010) (57 to 144 kJ mol^{-1}, Fig. 7). For all bulks examined, higher SFE surfaces have more-exothermic HAE values. Contrasting the lowest HAE value per each bulk shows that the lower HAE values correspond to intermediate Mg-contents, being generally lower for meta- and pyro-vanadate surfaces.

The initial C–H activation barriers of C_1–C_3 alkanes correlate with their corresponding HAE values (Fig. 8) with significantly less scatter than that observed for the correlation with VFE. Structural data suggests that HAE is a better descriptor than VFE because the addition of H* results in significantly less surface restructuring than in the presence of a vacancy. However, HAE correlations still show scatter that is absent in previous studies across other systems. For example, DFT+U calculations on C–H activation in alkanes (C_1–C_4) and alkanols (C_1–C_3) across a series of POM clusters ($H_3PMo_{12}O_{40}$, $H_4SiMo_{12}O_{40}$, $H_3PW_{12}O_{40}$, $H_4PVMo_{11}O_{40}$, and $H_4PVW_{11}O_{40}$) [82] demonstrate that the reactivity of surface oxygens could be described using a simple hydrogen addition energy (HAE), and that activation barriers could be predicted with a combination of these HAE values and the BDE of the reacting alkane or alkanol. An additional study on the dissociation of diatomic molecules across transition metal oxides (MO_2; M = Mo, Ir, Ru, Pt, and Ti) found a strong correlation between the activation energy for molecule dissociation and its corresponding dissociative adsorption [162]. This correlation, however, was only applicable to late-transition states, suggesting that resemblance between the electronic structure of the transition state and the descriptor plays a significant role when developing structure–function relationships for metal oxide surfaces.

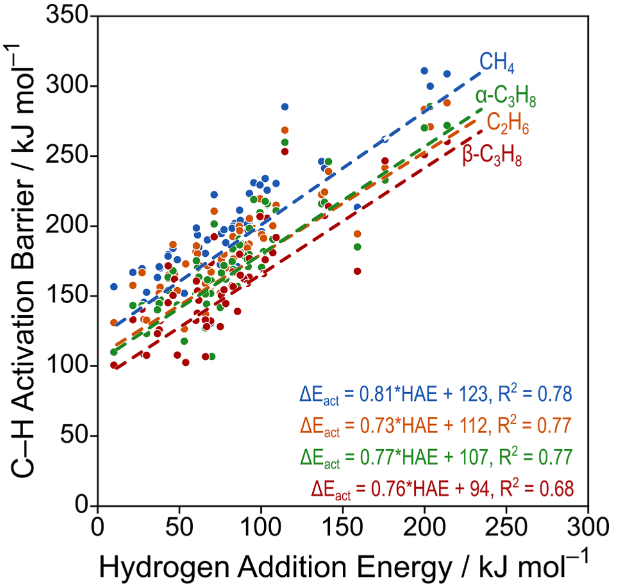

Fig. 8. Initial C–H activation barrier of methane (CH_4; blue), ethane (C_2H_6; orange), and propane (a-C_3H_8; green; b-C_3H_8; red) as a function of the hydrogen addition energies (HAE) across selected surfaces for V_2O_5, MgV_2O_6, t- and m-$Mg_2V_2O_7$, and $Mg_3V_2O_8$ bulks. Each data point corresponds to a unique surface oxygen atom. Electronic barriers (kJ/mol) are reported relative to the corresponding bare surface and gas phase alkane. Linear regressions with their corresponding R^2 values are also provided. (For interpretation of the references to colour in this figure legend, the reader is referred to the web version of this article.)

Contrasting the structures of H* calculations (used to calculate HAE) with their corresponding C–H activation transition state reveals that the orientation of some H* species relative to the surface is different from that of the transition state structure because of H-bonding that stabilizes H* species when oriented toward a vicinal O-atom. This is the result of hydrogen bonding interactions (e.g., Fig. 9a), which are absent in alkane activation transition states. As such, we attribute the existing scattering between HAE values and their corresponding C–H activation to the differences in geometry between the transition state and H* species due to H-bonding in V_2O_5 and Mg-vanadates. An approach that freezes H atoms in their respective transition state positions may yield a stronger correlation but would necessitate transition state geometries which reduce the utility of a descriptor, that should otherwise avoid the necessity of calculating a transition state structure. These considerations then prompt to use a chemical species that is isoelectronic to H* but absent of H-bonding, such as CH_3 addition energies.

An alternative descriptor to HAE is the methyl-addition energy (MAE). MAE values are estimated from the energy of reaction for:

$$MO + 1/4\ O_2 + CH_4 \rightarrow MO - CH_3 + 1/2\ H_2O \tag{4}$$

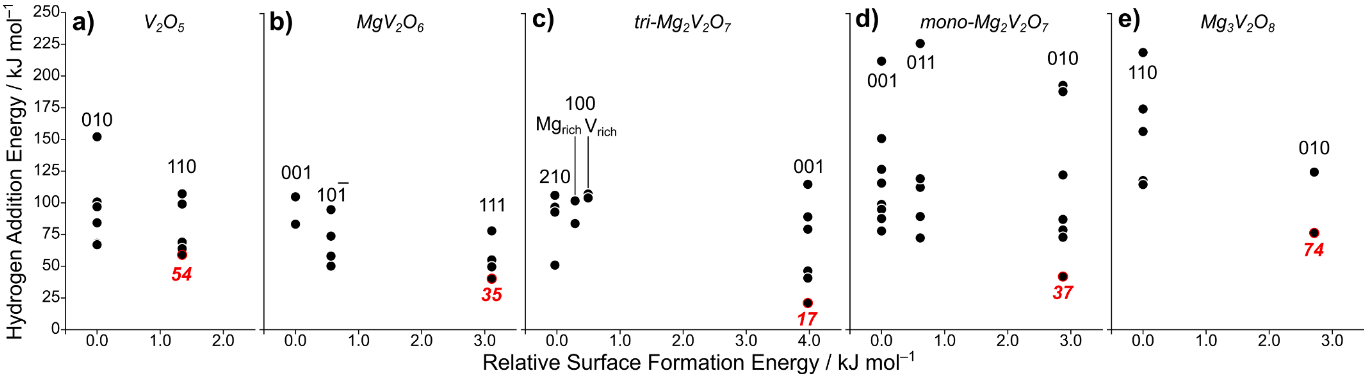

Fig. 7. Hydrogen addition energies (HAE) as a function of relative surface formation energies (SFE) across examined surfaces for a) V_2O_5, b) MgV_2O_6, c) triclinic $Mg_2V_2O_7$, d) monoclinic $Mg_2V_2O_7$, and e) $Mg_3V_2O_8$. Lattice planes are labeled by surface Miller index. Each data point corresponds to a vacancy from unique O lattice atoms. Two distinct terminations are shown for triclinic $Mg_2V_2O_7$ (1 0 0) surface.

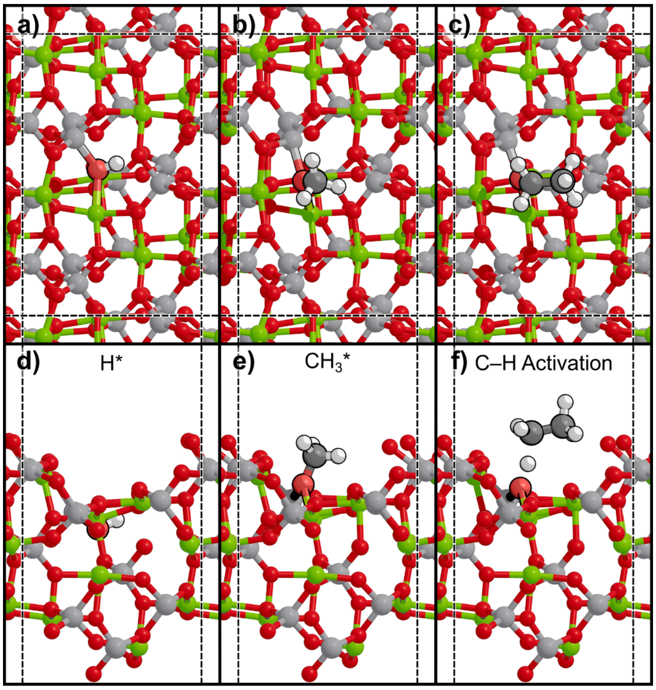

Fig. 9. Top and side views of H* (a,d), CH_3* (b,e), and ethane C–H activation transition state (c,f) structures on mono-$Mg_2V_2O_7$ (001) surface.

As such, MAE values in this work (Fig. S9) also serve as a proxy to MO–CH_3 formation during ODH of alkanes. MAE values in this work range from –133 to 80 kJ mol^{-1}, with average values across bulks of –61 kJ mol^{-1} for V_2O_5, –60 kJ mol^{-1} for MgV_2O_6, –64 kJ mol^{-1} for tri-$Mg_2V_2O_6$, –18 kJ mol^{-1} for mono-$Mg_2V_2O_6$, and 4 kJ mol^{-1} for $Mg_3V_2O_8$. Average values for MAE across bulks become less exothermic with increasing Mg-content, consistent with the average trend for HAE values that becomes more endothermic with increasing Mg-content. Methyl groups are isoelectronic to H atoms, cannot undergo H-bonding, and have some steric hindrances that may lead to methyl orientations that are more alike to the H atom orientations in C–H activation transition states as those H atoms are coordinated to the C atom in the incipient radical and thus similarly experience steric hindrances. Therefore, the methyl group preserves its orientation and thus resembles more the C–H activation transition state (Fig. 9).

Fig. 10 shows the MAE values along with their corresponding C–H activations for C_1–C_3 alkanes. There is significantly less scatter within these correlations against MAE values than against HAE (Fig. 8) or VFE (Fig. 6). As described above and seen in Fig. 9, this is likely because the scatter in the HAE correlations is caused by the ability of H* to H-bond with neighboring O atoms (but not in the C–H activation transition state) and that mismatch between the H* and C–H activation transition state is not present for CH_3* as it cannot H-bond.

The y-axis intercepts in these correlations of C–H activation energy vs. MAE decrease with increasing alkane chain length (CH_4, 228 > C_2H_6, 210 > C_3H_6 (terminal), 204 > C_3H_6 (central), 192). These values trend with the corresponding bond dissociation energies for C–H in these alkanes (CH_4, 465 kJ mol^{-1} > C_2H_6, 442 kJ mol^{-1} ~ α-C_3H_8, 443 kJ mol^{-1} > β-C_3H_8, 427 kJ mol^{-1}). This is consistent with our reported intercept values, as well as with previous work [82] on POM clusters that found BDE values to correlate with C–H activation barriers of alkanes, alkenes, and alkanols. These y-intercept values omit the impacts of dispersive corrections, which would be expected to decrease these effective activation barriers as those corrections will make alkane adsorptions more exothermic.

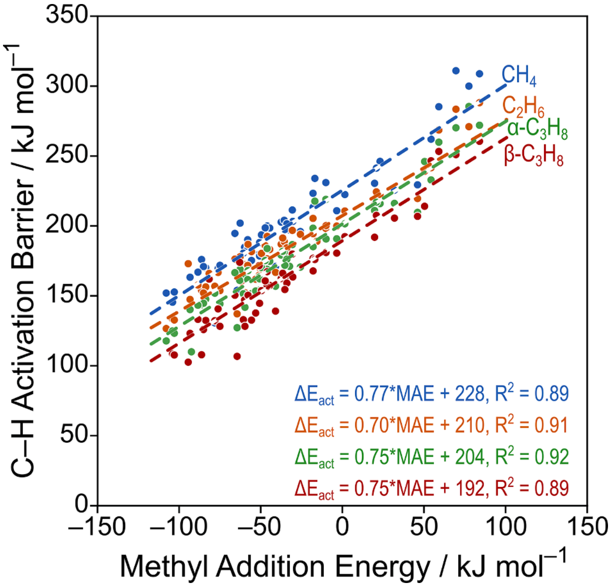

Fig. 10. Initial C–H activation barrier of methane (CH_4; blue), ethane (C_2H_6; orange), and propane (a-C_3H_8; green; b-C_3H_8; red) as a function of the hydrogen addition energies (HAE) across selected surfaces for V_2O_5, MgV_2O_6, tri- and mono-$Mg_2V_2O_7$, and $Mg_3V_2O_8$ bulks. Each data point corresponds to a unique surface oxygen atom. Electronic barriers (kJ mol^{-1}) are reported relative to the corresponding bare surface and gas phase alkane. Linear regressions with their corresponding R^2 values are also provided. (For interpretation of the references to colour in this figure legend, the reader is referred to the web version of this article.)

3.4. *Impact of electronic properties on initial C–H activation in alkanes*

3.4.1. *Constrained orbital DFT*

While the MAE was found to be a useful chemical descriptor for predicting the initial C–H activation barrier in C_1–C_3 alkanes, our interest is to elucidate surface features that describe C–H activation beyond the established correlations. To do so it would be more intuitive to have an electronic descriptor that relates the barrier to electronic changes occurring during the reaction. One such technique for deconvoluting the electronic transformation underlying chemical processes occurring on a catalytic surface is constrained orbital density functional theory (co-DFT), developed by Plaisance et al. [150] The co-DFT method allows one to perform fully self-consistent Kohn-Sham DFT calculations in the presence of certain constraints on the form and occupancy of one or more orbitals. This method should not be confused with the fundamentally different constrained density functional theory (CDFT) [151], which allows only constraints on the electron density. For example, one can use co-DFT to force a single half-filled orbital to localize on a single oxygen atom. We refer to the resulting energetic penalty for enforcing this constraint as the localization energy and use it as an electronic descriptor to correlate with the alkane activation barrier and methyl addition energy—shown to be the best chemical descriptor in Section 3.3—for a specific oxygen site on a surface. This approach has been used previously to demonstrate how the HAE on other 3*d* transition metal oxides is correlated to the electronic properties of the surface [150,163].

The rationale for using the localization energy as an electronic descriptor for methyl adsorption energy can be understood by examining the thermodynamic cycle illustrated in Scheme 1.

The overall chemical process can be decomposed into three theoretical steps: surface distortion, orbital localization, and MO—CH_3 bond formation. The first step involves a geometric distortion of the atoms from the pristine surface to the positions they relax to upon addition of the methyl. This process will be associated with an energy penalty that we refer to as the distortion energy, which is defined as,

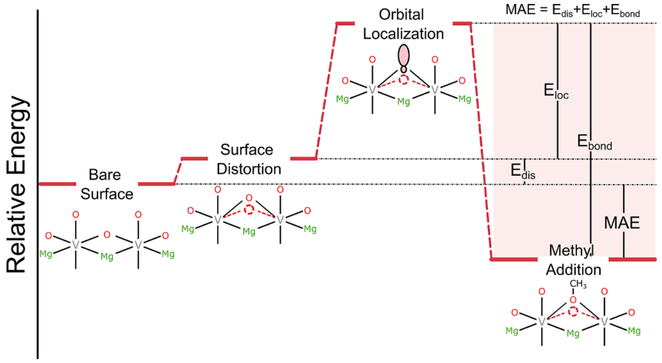

Scheme 1. Thermochemical cycle for CH_3 addition to Mg-vanadate surfaces. The methyl-addition energy (MAE) is decomposed into three theoretical steps: (1) geometric distortion (E_{dis}), (2) constrained orbital localization (E_{loc}), and (3) CH_3 bond formation with surface (E_{bond}) so that MAE = E_{dis} + E_{loc} + E_{bond}. States are at scale (i.e., platforms are shown scaled to their corresponding average value).

$$E_{dis} = E(MO, dis) - E(MO) \tag{5}$$

Here, $E(MO, dis)$ is the energy of the structure obtained by deleting the methyl fragment from the relaxed MO—CH_3 structure. Likewise, $E(MO)$ is the energy of the relaxed MO structure. Once the geometry of the surface has distorted, the electronic structure must also distort electronically in preparation for forming the MO—CH_3 bond. This is done by constraining a half-filled orbital to localize onto the oxygen atom that eventually binds to the methyl fragment. We use the term 'half-filled' to denote a pair of spin orbitals that contain half of a spin up electron and half of a spin down electron. The co-DFT method is used to compute the energy of the localized electronic configuration $E(surf, loc)$, which is then used to define the localization energy,

$$E_{loc} = E(MO, loc) - E(MO, dis) \tag{6}$$

In the final step of the thermodynamic cycle, a methyl radical produced from CH_4 and O_2 forms the MO—CH_3 bond with the localized oxygen orbital by the process,

$$CH_4 + \frac{1}{4}O_2 + (MO)_{loc} \rightarrow MO - CH_3 + \frac{1}{2}H_2O \tag{7}$$

The energy of this process, defined as the bond energy, is given by,

$$E_{bond} = E(MO - CH_3) - E(MO, loc) - E(CH_3) \tag{8}$$

where the energy of a methyl fragment is given by,

$$E(CH_3) = E(CH_4) + \frac{1}{4}E(O_2) - \frac{1}{2}E(H_2O) \tag{9}$$

Altogether, the methyl addition energy is given by the sum of the three contributions,

$$E_{MAE} = E_{dis} + E_{loc} + E_{bond} \tag{10}$$

The rationale for this particular decomposition is that the bond energy is expected to exhibit minimal variation between different sites and surfaces. The reason for this is that a highly localized σ bond exists between the surface oxygen and the methyl carbon in MO—CH_3. The associated σ bonding orbital consists of a linear combination of sp^{λ} hybrid orbitals on the oxygen and carbon atoms. If the methyl fragment is 'deleted', one is left with half an electron of each spin remaining in the oxygen hybrid orbital with the other half of each electron accompanying the methyl fragment. The resulting state of the surface is equivalent to the surface with a half-filled orbital localized on the oxygen atom. The energy required to break the σ bond in this way is therefore equivalent to E_{bond} defined above and will mainly depend on the Hamiltonian overlap integral between the two hybrid orbitals forming the bond. This integral will in turn depend primarily on the composition of the hybrid orbitals, which we find to vary only slightly between the different sites and surfaces. As a result, most of the variation in the methyl addition energy is expected to arise from variations in the localization energy and distortion energy, the latter being a geometric descriptor while the former is an electronic descriptor.

A difficulty in using the localization energy as an electronic descriptor is that one must specify the form of the localized oxygen orbital. In general, it will be a linear combination of the 2s and three 2p atomic orbitals on the oxygen atom:

$$h = a_s s + \left(1 - a_s^2\right)^{1/2}\left(b_x p_x + b_y p_y + b_z p_z\right) \tag{11}$$

The atomic orbitals are taken as the Löwdin-orthogonalized quasi-atomic orbitals calculated for the (electronically) unconstrained distorted surface. The quasi-atomic orbitals form a minimal atomic orbital basis set that exactly reproduces the ground state properties of the system computed in a large plane wave basis set. They are computed using an in-house version of VASP into which we have previously implemented the quasi-atomic orbital method along with co-DFT. The s character of the localized orbital is fixed to a value of $a_s = 0.52$, while the direction of the normalized p vector $\left(b_x, b_y, b_z\right)$ is taken to lie along the O—C bond in the optimized MO—CH_3 structure. The value of a_s was determined by performing a bond decomposition analysis on the O—C bond for the six different oxygen sites among the examined V_2O_5 surfaces. The resulting values of a_s fall in the range 0.50–0.56, with an average value of 0.52. As these six structures cover the full range of oxygen coordination environments (atop, bridge, and 3-fold), we expect the calculated values of a_s to give a good estimate of the variation of this quantity between the 64 different sites and surfaces examined in this study. The fact that a_s lies in a narrow range for such disparate chemical environments lends confidence to the use of a single value of 0.52 for all sites.

Fig. 11 shows that the methyl addition energy is indeed well correlated with the sum of the distortion and localization energies for bridge and 3-fold oxygen sites, accounting for 92–93 % of the variation. This is the same quality as the correlation between the C—H activation barrier and the methyl addition energy, which is also shown in Fig. 11 for C_1–C_3 alkanes. However, there is no significant correlation for atop oxygen sites. Any deviations from the correlation are necessarily due to variations in E_{bond} between the different sites and surfaces.

Overall, the established thermochemical cycle reveals the connection between the catalyst surface and how the reactivity can be controlled by the structure. For example, the average surface distortion penalty values (Fig. 11c, blue) per bulk material are 1.02 eV for V_2O_5, 1.18 eV for MgV_2O_6, 0.99 eV for t-$Mg_2V_2O_7$, 1.19 eV for m-$Mg_2V_2O_7$, and 1.36 eV for $Mg_3V_2O_8$. These values suggest that, in general, surface distortion is more difficult in Mg-vanadates with higher Mg-content. Extending the analysis to the electronic localization components (Fig. 11c, red), the corresponding average values per bulk are 7.52 eV for V_2O_5, 7.10 eV for MgV_2O_6, 7.26 eV for t-$Mg_2V_2O_7$, 7.48 eV for m-$Mg_2V_2O_7$, and 7.84 eV for $Mg_3V_2O_8$. These values also indicate that bond localization is generally more difficult in lattice O atoms within higher Mg-content surfaces. Thus, in the context of the descriptor we identified, the activity of Mg-vanadate surfaces is related to the catalyst structure in (1) its ability to distort and thus accommodate CH_3* and C–H activation transition states and (2) its ability to localize electrons in the lattice O atoms mediating the corresponding CH_3* adsorptions and C–H activation transition states. As such, we rationalize that the activity of Mg-vanadate surfaces is governed by geometric and electronic distortions that become generally more difficult with increasing Mg content in these systems. Overall, differences in localization energy are more significant than those for distortion energy among bulks, suggesting that while Mg vanadates similarly distort to accommodate adsorbates and

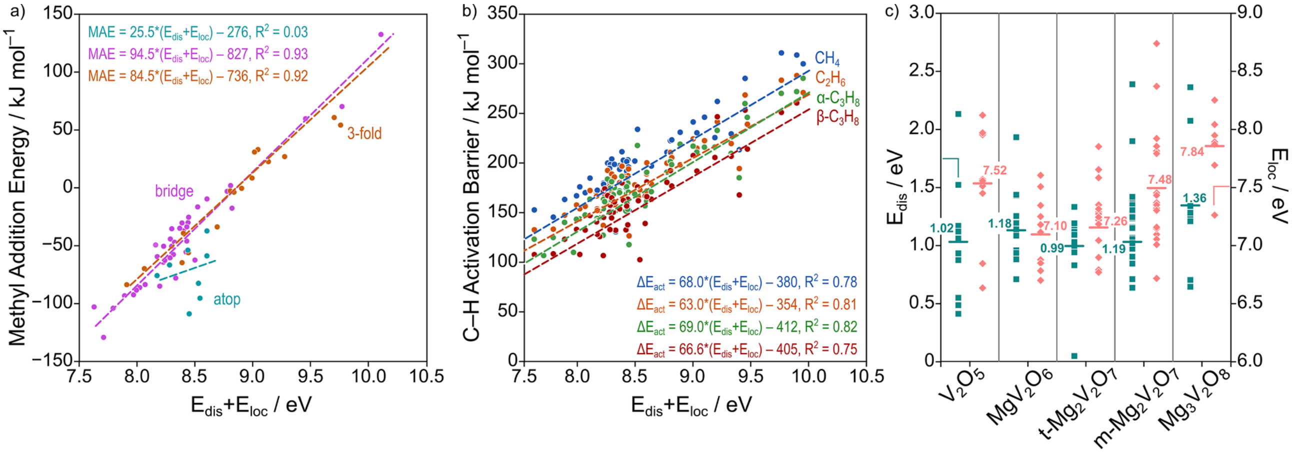

Fig. 11. a)Methyl-addition energies (MAE) as a function of $E_{dis} + E_{loc}$ for atop (blue), bridged (purple) and 3-fold (orange) oxygens across V_2O_5 and Mg-vanadates selected surfaces. b) Initial C–H activation barrier of methane (CH_4; blue), ethane (C_2H_6; orange), and propane (a-C_3H_8; green; b-C_3H_8; red) as a function of $E_{dis} + E_{loc}$ across selected surfaces for V_2O_5, Mg-vanadates bulks. Each data point corresponds to a unique surface oxygen atom. Electronic barriers (kJ mol^{-1}) are reported relative to the corresponding bare surface and gas phase alkane. c) Individual values for E_{dis} (turquoise) and E_{loc} (pink) for all the unique O-atoms as a function of bulk material. Averages values are also provided. (For interpretation of the references to colour in this figure legend, the reader is referred to the web version of this article.)

transition states, the electronic configuration plays a larger role in the observed differences in reactivity toward C–H activation of alkanes.

3.4.2. *Partial density of states*

Considering the effectiveness of using the localization energy to correlate with the MAE, it is worth exploring whether a simpler descriptor based on partial densities of states (PDOS) could also serve this purpose. In fact, one can construct a non-self-consistent quantity from the PDOS (Fig. S10) that is analogous to the reported localization energy:

$$E_{\mathrm{loc}}^{\mathrm{PDOS}} = E_{\mathrm{V,3d}}^{\mathrm{unocc}} - E_{\mathrm{O,2p}}^{\mathrm{occ}} \tag{12}$$

where $E_{\mathrm{V,3d}}^{\mathrm{unocc}}$ is the average energy of the V 3*d* states above the Fermi level and $E_{\mathrm{O,2p}}^{\mathrm{occ}}$ is the average energy of the O 2*p* states below the Fermi level. By non-self-consistent, we mean that the energy does not include changes in electron–electron repulsion that accompany the localization process. To compute $E_{\mathrm{V,3d}}^{\mathrm{unocc}}$, we use the PDOS of the vanadium atom onto which the electron is found to localize upon methyl addition,

$$E_{\mathrm{V,3d}}^{\mathrm{unocc}} = \int_{E_{\mathrm{F}}}^{E_{\mathrm{cb,max}}} dE\ E\ \rho_{\mathrm{V,3d}}(E) \tag{13}$$

where $E_{\mathrm{cb,max}}$ is the maximum energy of the conduction band. Likewise, to compute $E_{\mathrm{O,2p}}^{\mathrm{occ}}$ we use the PDOS of the O atom onto which the methyl is added,

$$E_{\mathrm{O,2p}}^{\mathrm{occ}} = \int_{E_{\mathrm{vb,min}}}^{E_{\mathrm{F}}} dE\ E\ \rho_{\mathrm{O,2p}}(E) \tag{14}$$

where $E_{\mathrm{vb,min}}$ is the minimum energy of the valence band. The rationale for using the quantity in Eq. (12) can be understood by decomposing the localization process into three steps. First, a lone pair localizes onto the O atom with an associated energy $E_{\mathrm{O,2p}} - E_{\mathrm{O,2p}}^{\mathrm{occ}}$, where $E_{\mathrm{O,2p}}$ is the average energy of both occupied and unoccupied 2p states on the O atom,

$$E_{\mathrm{O,2p}} = \int_{E_{\mathrm{vb,min}}}^{E_{\mathrm{cb,max}}} dE\ E\ \rho_{\mathrm{O,2p}}(E) \tag{15}$$

Then, a hole pair localizes onto the V atom with an associated energy $E_{\mathrm{V,3d}} - E_{\mathrm{V,3d}}^{\mathrm{unocc}}$, where $E_{\mathrm{V,3d}}$ is the average energy of both occupied and unoccupied 3d states on the V atom,

$$E_{\mathrm{V,3d}} = \int_{E_{\mathrm{vb,min}}}^{E_{\mathrm{cb,max}}} dE\ E\ \rho_{\mathrm{V,3d}}(E) \tag{16}$$

Finally, one electron is transferred from O lone pair to the empty V orbital, contributing an energy $E_{\mathrm{V,3d}} - E_{\mathrm{O,2p}}$.

The correlation between the methyl addition energy and the non-self-consistent localization energy computed by Eq. (12) is shown in Fig. 12, where it can be seen that the correlation is present, but with significant scatter. This is because of two effects that are absent from $E_{\mathrm{loc}}^{\mathrm{PDOS}}$. First, this quantity does not include the distortion energy, which was seen in the last section to make a significant contribution to the MAE. Second, this quantity does not include the change in electron–electron repulsion that accompanies the localization process.

In general, co-DFT methodology results in better correlations than non-self-consistent interpretation of PDOS calculations. The deconstruction of MAE as a convolution of distortion, localization, and bonding energies provides both geometric and electronic insights to MAE as a chemical descriptor. Distortion energies are shown to play a significant role; however, surface distortions are only known after MAE calculations are performed. Moreover, localization energies serve as a better proxy for surface reducibility than traditional VFE descriptors. Since the addition of distortion and localization energies correlates with MAE values, we have successfully identified the role of surface distortion and electronic rearrangement during C–H activation in these systems. As such, we not only report MAE-based descriptors as a useful predictor of initial C–H activation of alkanes in metal oxides, but also provide rationale for its decomposition into geometric and electronic components.

4. Conclusions

V_2O_5 and $Mg_xV_2O_{5+x}$ catalysts contain VO_4 tetrahedra within their oxide lattice and expose reactive VO_x species at their surfaces. As the Mg:V ratio increases, VO_4 tetrahedra go from forming edge-sharing chains in meta-vanadate (MgV_2O_6) to corner-sharing chains in pyrovanadate ($Mg_2V_2O_7$) to being completely isolated from each other in ortho-vanadate ($Mg_3V_2O_8$). The reactivity for the initial C–H activation in C_1–C_3 alkanes was investigated on V_2O_5 and Mg-vanadate ($Mg_xV_2O_{5+x}$, x = 1–3) surfaces using DFT+U calculations. ODH reactions of alkanes across these oxides are thought to proceed via homolytic C–H activation of the alkane, with this being the rate

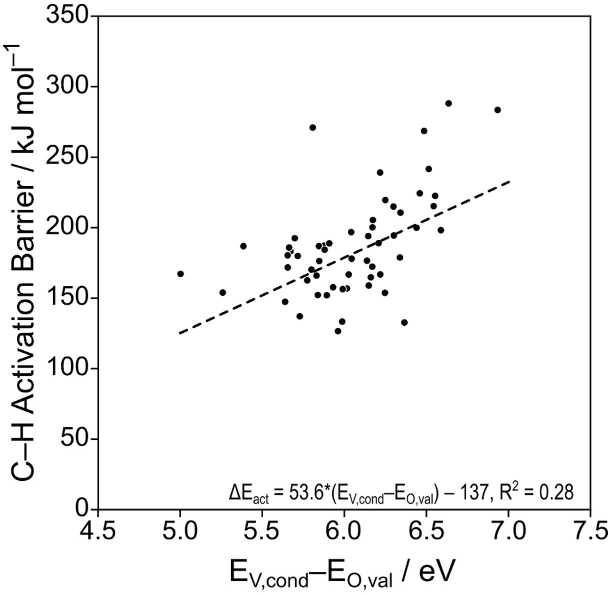

Fig. 12. Effective C–H activation barriers in ethane (C_2H_6) as a function of the non-self-consistent localization energy. The band energy is defined here as the average of the band energies weighted by their respective occupancies.

determining step. C–H activation occurs at lattice oxygen, which abstracts hydrogen from the alkane, forming a hydroxyl (OH) species and an alkyl radical. The transition states for initial C–H activation were explored for CH_4, C_2H_6, and C_3H_8 (for propane, at both the terminal and central C atoms). Calculated barriers were found to be qualitatively consistent with kinetic data and surface reducibility proxies (temperature programmed reduction and *in situ* electrical conductivity measurements) that suggest that reactivity on Mg-vanadate surfaces decreases with increasing Mg:V ratios.

Initial C–H activation of C_1–C_3 alkanes was examined across 64 surface O atoms (active sites) present across these 14 surfaces, and these O atoms range in coordination (from atop to three-fold) and chemical environment (e.g., in both Mg–O–V and V–O–V bridge sites). Alkane activation barriers vary among lattice O atoms within each surface, suggesting that the reactivity of Mg-vanadate surfaces is governed by oxygen-specific features rather than surface features. When considering oxygen atom coordination and neighbors, it was found that C–H activation barriers are generally lower at undercoordinated O atoms (atop $<$ bridged $<$ three-fold), and that barriers generally increase with increasing Mg:V ratios (e.g., V–O–V $<$ Mg–O–V for bridging O atoms).

Oxygen vacancy formation energy (VFE), hydrogen addition energy (HAE), and methyl addition energy (MAE) were calculated as proxies of surface O atom reducibility and thus reactivity. C–H activation barriers are generally higher on oxygen atoms with larger VFE values (i.e., less reducible), but significant scatter—likely resulting from surface restructuring during optimization—makes VFE a weak predictor for C–H activation of alkanes. C–H activation barriers in C_1–C_3 alkanes do correlate with their corresponding HAE values, as H* species emulate the H radical coming from the C–H activation on alkanes. MAE values, however, were found to outperform HAE as a reactivity descriptor. This is because the proximity of surface oxygen atoms in Mg-vanadates enables H-bonding in H* species such that optimized orientation of H* no longer resembles C–H activation transition states, weakening the ability of HAE as a descriptor. CH_3* groups, while being electronically similar to H*, incur steric hindrances that resemble transition states and cannot H-bond. As such, MAE values are better proxies for reactivity toward C–H activation of C_1–C_3 alkanes because CH_3 groups better resemble C–H transition state structures across V_2O_5 and Mg-vanadate surfaces. In addition, we show that MAE values can be deconvoluted into a thermochemical cycle that includes surface distortion and electronic localization energies that reveal that the ability of Mg-vanadate catalysts to mediate C–H activation transition states is intimately related to its ability to geometrically and electronically distort to accommodate C–H activation transition states. This, in turn, provides rationale for the observed reactivities in Mg-vanadates and the role of Mg:V content on alkane ODH reaction rates.

To summarize, we report a MAE as an alternate descriptor for C–H activation on metal oxides. This descriptor was transferable to not only surfaces of varying Mg:V ratio, but also to a diverse set of active sites with varying O coordination environment. Furthermore, this work provides the first fundamental theoretical study of alkane ODH on Mg-vanadates and corroborates with DFT methods prior-observed reactivity trends among these materials while identifying low-energy surfaces of interest. This lays the groundwork for future studies of Mg-vanadate reactivity, selectivity, with and without metal dopants.

CRediT authorship contribution statement

Hansel Montalvo-Castro: Data curation, Formal analysis, Investigation, Writing – original draft, Writing – review & editing, Validation, Visualization. **Álvaro Loaiza-Orduz:** Data curation, Formal analysis. **Randall J. Meyer:** Conceptualization, Funding acquisition, Project administration, Resources, Software, Writing – review & editing. **Craig Plaisance:** Conceptualization, Formal analysis, Methodology, Resources, Software, Supervision, Validation, Writing – original draft, Writing – review & editing. **David Hibbitts:** Conceptualization, Data curation, Formal analysis, Funding acquisition, Investigation, Methodology, Project administration, Resources, Software, Supervision, Validation, Writing – review & editing.

Declaration of competing interest

The authors declare the following financial interests/personal relationships which may be considered as potential competing interests: David Hibbitts reports financial support and equipment, drugs, or supplies were provided by ExxonMobil Research and Engineering Company Annandale. If there are other authors, they declare that they have no known competing financial interests or personal relationships that could have appeared to influence the work reported in this paper.

Acknowledgements

This work was funded by ExxonMobil Technology and Engineering Company and partially funded by the National Science Foundation (NSF-#CHE-1954611). Computational resources were provided by ExxonMobil, University of Florida Research Computing, and the Louisiana State University High-Performance Computing.

Appendix A. Supplementary data

Supplementary data to this article can be found online at https://doi.org/10.1016/j.jcat.2024.115800.

Data availability

Data will be made available on request.

References

[1] E.A. Mamedov, V. Cortés Corberán, Oxidative dehydrogenation of lower alkanes on vanadium oxide-based catalysts. The present state of the art and outlooks, Appl. Catal. A 127 (1995) 1–40, https://doi.org/10.1016/0926-860X(95)00056-9.

[2] J.J.H.B. Sattler, J. Ruiz-Martinez, E. Santillan-Jimenez, B.M. Weckhuysen, Catalytic dehydrogenation of light alkanes on metals and metal oxides, Chem. Rev. 114 (2014) 10613–10653, https://doi.org/10.1021/cr5002436.

[3] A. Darvishi, R. Davand, F. Khorasheh, M. Fattahi, Modeling-based optimization of a fixed-bed industrial reactor for oxidative dehydrogenation of propane, Chin. J. Chem. Eng. 24 (2016) 612–622, https://doi.org/10.1016/j.cjche.2015.12.018.

[4] A.H. Elbadawi, M.S. Osman, S.A. Razzak, M.M. Hossain, VO_x-Nb/La-γAl_2O_3 catalysts for oxidative dehydrogenation of ethane to ethylene, J. Taiwan Inst. Chem. Eng. 61 (2016) 106–116, https://doi.org/10.1016/j.jtice.2016.01.003.

[5] F. Cavani, N. Ballarini, A. Cericola, Oxidative dehydrogenation of ethane and propane: How far from commercial implementation? Catal. Today. 127 (2007) 113–131, https://doi.org/10.1016/j.cattod.2007.05.009.

[6] A.A. Ayandiran, I.A. Bakare, H. Binous, S. Al-Ghamdi, S.A. Razzak, M.M. Hossain, Oxidative dehydrogenation of propane to propylene over VO_x /CaO–γ-Al_2O_3 using lattice oxygen, Catal. Sci. Technol. 6 (2016) 5154–5167, https://doi.org/10.1039/C6CY00078A.

[7] M.M. Bhasin, Is True Ethane Oxydehydrogenation Feasible?, Springer Science and Business Media LLC. (2003). doi: 10.1023/a:1024884623238.

[8] S. Wang, Z.H. Zhu, Catalytic conversion of alkanes to olefins by carbon dioxide oxidative dehydrogenation - A review, Energy Fuels. 18 (2004) 1126–1139, https://doi.org/10.1021/ef0340716.

[9] G. Li, C. Liu, X. Cui, Y. Yang, F. Shi, Oxidative dehydrogenation of light alkanes with carbon dioxide, Green Chem. 23 (2021) 689–707, https://doi.org/10.1039/D0GC03705B.

[10] D. Chen, A. Holmen, Z. Sui, X. Zhou, Carbon mediated catalysis: a review on oxidative dehydrogenation, Chin. J. Catal. 35 (2014) 824–841, https://doi.org/10.1016/S1872-2067(14)60120-0.

[11] C.A. Carrero, R. Schloegl, I.E. Wachs, R. Schomaecker, Critical literature review of the kinetics for the oxidative dehydrogenation of propane over well-defined supported vanadium oxide catalysts, ACS Catal. 4 (2014) 3357–3380, https://doi.org/10.1021/cs5003417.

[12] R. Grabowski, Kinetics of oxidative dehydrogenation of C_2–C_3 alkanes on oxide catalysts, Catal. Rev. 48 (2006) 199–268, https://doi.org/10.1080/01614940600631413.

[13] D.P. Melnikov, A.A. Novikov, A.P. Glotov, M.V. Reshetina, E.M. Smirnova, H. Q. Wang, V.A. Vinokurov, Dehydrogenation of light alkanes (A review), Pet. Chem. 62 (2022) 1027–1046, https://doi.org/10.1134/S096554412209006.

[14] M. Baerns, O. Buyevskaya, Simple chemical processes based on low molecular-mass alkanes as chemical feedstocks, Catal. Today. 45 (1998) 13–22, https://doi.org/10.1016/S0920-5861(98)00231-4.

[15] J.H. Miller, L. Bui, A. Bhan, Pathways, mechanisms, and kinetics: a strategy to examine byproduct selectivity in partial oxidation catalytic transformations on reducible oxides, React. Chem. Eng. (2019), https://doi.org/10.1039/C8RE00285A.

[16] X. Rozanska, R. Fortrie, J. Sauer, Oxidative dehydrogenation of propane by monomeric vanadium oxide sites on silica support, J. Phys. Chem. C 111 (2007) 6041–6050, https://doi.org/10.1021/jp071409e.

[17] S. Rostom, H. de Lasa, Propane oxidative dehydrogenation on vanadium-based catalysts under oxygen-free atmospheres, Catalysts 10 (2020) 418, https://doi.org/10.3390/catal10040418.

[18] S. Rostom, H.I. de Lasa, Propane oxidative dehydrogenation using consecutive feed injections and fluidizable $VO_x/\gamma Al_2O_3$ and VO_x/ZrO_2-Al_2O_3 catalysts, Ind. Eng. Chem. Res. 56 (2017) 13109–13124, https://doi.org/10.1021/acs.iecr.7b01369.

[19] M.M. Hossain, Kinetics of oxidative dehydrogenation of propane to propylene using lattice oxygen of VO_x/CaO/γAl_2O_3 catalysts, Ind. Eng. Chem. Res. 56 (2017) 4309–4318, https://doi.org/10.1021/acs.iecr.7b00759.

[20] S.A. Al-Ghamdi, H.I. de Lasa, Propylene production via propane oxidative dehydrogenation over VO_x/γ-Al_2O_3 catalyst, Fuel 128 (2014) 120–140, https://doi.org/10.1016/j.fuel.2014.02.033.

[21] K. Fukudome, N. Ikenaga, T. Miyake, T. Suzuki, Oxidative dehydrogenation of alkanes over vanadium oxide prepared with $V(t\text{-}BuO)_3O$ and $Si(OEt)_4$ in the presence of polyethyleneglycol, Catal. Today. 203 (2013) 10–16, https://doi.org/10.1016/j.cattod.2012.04.042.

[22] K. Fukudome, N. Ikenaga, T. Miyake, T. Suzuki, Oxidative dehydrogenation of propane using lattice oxygen of vanadium oxides on silica, Catal. Sci. Technol. 1 (2011) 987, https://doi.org/10.1039/c1cy00115a.

[23] M.A. Bañares, Supported metal oxide and other catalysts for ethane conversion: a review, Catal. Today. 51 (1999) 319–348, https://doi.org/10.1016/S0920-5861(99)00053-X.

[24] S.T. Oyama, A.M. Gaffney, J.E. Lyons, R.K. Grasselli, Third World Congress on Oxidation Catalysis, second ed., Elsevier S & T, Amsterdam, 1997.

[25] A. Galli, J.M. López Nieto, A. Dejoz, M.I. Vazquez, The effect of potassium on the selective oxidation of *n*-butane and ethane over Al_2O_3-supported vanadia catalysts, Catal. Lett. 34 (1995) 51–58, https://doi.org/10.1007/BF00808321.

[26] A.H. Elbadawi, M.S. Ba-Shammakh, S. Al-Ghamdi, S.A. Razzak, M.M. Hossain, H. I. de Lasa, Phenomenologically based kinetics of ODH of ethane to ethylene using lattice oxygen of VO_x/Al_2O_3–ZrO_2 catalyst, Chem. Eng. Res. Des. 117 (2017) 733–745, https://doi.org/10.1016/j.cherd.2016.11.015.

[27] A.H. Elbadawi, M.S. Ba-Shammakh, S. Al-Ghamdi, S.A. Razzak, M.M. Hossain, H. I. de Lasa, A fluidizable VO_x/γ–Al_2O_3–ZrO_2 catalyst for the ODH of ethane to ethylene operating in a gas phase oxygen free environment, Chem. Eng. Sci. 145 (2016) 59–70, https://doi.org/10.1016/j.ces.2016.01.050.

[28] A.H. Elbadawi, M.S. Ba-Shammakh, S. Al-Ghamdi, S.A. Razzak, M.M. Hossain, Reduction kinetics and catalytic activity of VO_x/γ-Al_2O_3-ZrO_2 for gas phase oxygen free ODH of ethane, Chem. Eng. J. 284 (2016) 448–457, https://doi.org/10.1016/j.cej.2015.08.048.

[29] H.H. Kung, M.C. Kung, Oxidative dehydrogenation of alkanes over vanadium-magnesium-oxides, Appl. Catal. A 157 (1997) 105–116, https://doi.org/10.1016/S0926-860X(97)00028-8.

[30] T. Blasco, J.M. Lopez-Nieto, Oxidative dyhydrogenation of short chain alkanes on supported vanadium oxide catalysts, Appl. Catal. A 157 (1997) 117–142, https://doi.org/10.1016/S0926-860X(97)00029-X.

[31] M.D. Argyle, K. Chen, A.T. Bell, E. Iglesia, Effect of catalyst structure on oxidative dehydrogenation of ethane and propane on alumina-supported vanadia, J. Catal. 208 (2002) 139–149, https://doi.org/10.1006/jcat.2002.3570.

[32] E. Thorsteinson, T.P. Wilson, P.H. Kasai, The oxidative dehydrogenation of ethane over catalysts containing mixed oxides of molybdenum and vanadium, J. Catal. 52 (1978) 116–132, https://doi.org/10.1016/0021-9517(78)90128-8.

[33] J. Le Bars, A. Auroux, M. Forissier, J.C. Vedrine, Active sites of V_2O_5/γ-Al_2O_3 catalysts in the oxidative dehydrogenation of ethane, J. Catal. 162 (1996) 250–259, https://doi.org/10.1006/jcat.1996.0282.

[34] J. Le Bars, J.C. Védrine, A. Auroux, S. Trautmann, M. Baerns, Microcalorimetric and infrared studies of the acid-base properties of V_2O_5/γ-Al_2O_3 catalysts, Appl. Catal. A 119 (1994) 341–354, https://doi.org/10.1016/0926-860X(94)85201-4.

[35] J. Santamaría-González, J. Luque-Zambrana, J. Mérida-Robles, P. Maireles-Torres, A. Jiménez-López, Catalytic behavior of vanadium-containing mesoporous silicas in the oxidative dehydrogenation of propane, Catal. Lett. (2012).

[36] X. Gao, M.A. Bañares, I.E. Wachs, Ethane and n-butane oxidation over supported vanadium oxide catalysts: An *in Situ* UV–visible diffuse reflectance spectroscopic investigation, J. Catal. 188 (1999) 325–331, https://doi.org/10.1006/jcat.1999.2647.

[37] K. Chen, S. Xie, A.T. Bell, E. Iglesia, Structure and properties of oxidative dehydrogenation catalysts based on MoO_3/Al_2O_3, J. Catal. 198 (2001) 232–242, https://doi.org/10.1006/jcat.2000.3125.

[38] A. Khodakov, B. Olthof, A.T. Bell, E. Iglesia, Structure and catalytic properties of supported vanadium oxides: support effects on oxidative dehydrogenation reactions, J. Catal. 181 (1999) 205–216, https://doi.org/10.1006/jcat.1998.2295.

[39] F. Arena, F. Frusteri, A. Parmaliana, How oxide carriers affect the reactivity of V_2O_5 catalysts in the oxidative dehydrogenation of propane, Springer Science and Business Media LLC, 1999. doi: 10.1023/a:1019074016773.

[40] A. Corma, J.M. López-Nieto, N. Paredes, M. Pérez, Y. Shen, H. Cao, S.L. Suib, Oxidative Dehydrogenation Of Propane Over Supported-Vanadium Oxide Catalysts, in: New Developments in Selective Oxidation by Heterogeneous Catalysis, Elsevier, 1992: pp. 213–220. doi: 10.1016/S0167-2991(08)61673-0.

[41] M. Martinez-Huerta, X. Gao, H. Tian, I. Wachs, J. Fierro, M. Banares, Oxidative dehydrogenation of ethane to ethylene over alumina-supported vanadium oxide catalysts: Relationship between molecular structures and chemical reactivity, Catal. Today. 118 (2006) 279–287, https://doi.org/10.1016/j.cattod.2006.07.034.

[42] Z. Wu, H.-S. Kim, P.C. Stair, S. Rugmini, S.D. Jackson, On the structure of vanadium oxide supported on aluminas: UV and visible raman spectroscopy, UV-visible diffuse reflectance spectroscopy, and temperature-programmed reduction studies, J. Phys. Chem. b. 109 (2005) 2793–2800, https://doi.org/10.1021/jp046011m.

[43] F. Klose, T. Wolff, H. Lorenz, A. Seidelmorgenstern, Y. Suchorski, M. Piorkowska, H. Weiss, Active species on γ-alumina-supported vanadia catalysts: nature and reducibility, J. Catal. 247 (2007) 176–193, https://doi.org/10.1016/j.jcat.2007.01.013.

[44] H.H. Kung, Oxidative dehydrogenation of light (C_2 to C_4) alkanes, in: Advances in Catalysis , Elsevier, 1994, pp. 1–38. doi: 10.1016/S0360-0564(08)60655-0.

[45] K. Chen, E. Iglesia, A.T. Bell, Kinetic isotopic effects in oxidative dehydrogenation of propane on vanadium oxide catalysts, J. Catal. 192 (2000) 197–203, https://doi.org/10.1006/jcat.2000.2832.

[46] A. Dinse, B. Frank, C. Hess, D. Habel, R. Schomäcker, Oxidative dehydrogenation of propane over low-loaded vanadia catalysts: Impact of the support material on kinetics and selectivity, J. Mol. Catal. A: Chem. 289 (2008) 28–37, https://doi.org/10.1016/j.molcata.2008.04.007.

[47] M. Jin, P. Lu, G.X. Yu, Oxidative dehydrogenation of cyclohexane over Mg-V-O catalysts prepared via citriate complexation, AMR 284–286 (2011) 692–696, https://doi.org/10.4028/www.scientific.net/AMR.284-286.692.

[48] V. Palma, D. Sannino, V. Vaiano, P. Ciambelli, Fluidized-bed reactor for the intensification of gas-phase photocatalytic oxidative dehydrogenation of cyclohexane, Ind. Eng. Chem. Res. 49 (2010) 10279–10286, https://doi.org/10.1021/ie1005383.

[49] A.A. Vedyagin, I.V. Mishakov, E.V. Ilyina, A step forward in the preparation of V-Mg–O catalysts for oxidative dehydrogenation of propane, J. Solgel Sci. Technol. 97 (2021) 117–125, https://doi.org/10.1007/s10971-020-05438-1.

[50] A. Corrna, J.M.L. Nieto, N. Parades, A. Dejoz, I. Vazquez, Oxidative dehydrogenation of propane and n-butane on V-Mg based catalysts, in: New Developments in Selective Oxidation II, Proceedings of the Second World Congress and Fourth European Workshop Meeting, Elsevier, 1994, pp. 113–123. doi: 10.1016/S0167-2991(08)63403-5.

[51] J. Pless, B. Bardin, H.S. Kim, D. Ko, M. Smith, R. Hammond, P. Stair, K. Poeppelmeier, Catalytic oxidative dehydrogenation of propane over Mg–V/Mo oxides, J. Catal. 223 (2004) 419–431, https://doi.org/10.1016/j.jcat.2004.01.023.

[52] S.A. Korili, P. Ruiz, B. Delmon, Oxidative dehydrogenation of n-pentane on magnesium vanadate catalysts, Catal. Today. 32 (1996) 229–235, https://doi.org/10.1016/S0920-5861(96)00182-4.

[53] O.S. Owen, M.C. Kung, H.H. Kung, The effect of oxide structure and cation reduction potential of vanadates on the selective oxidative dehydrogenation of butane and propane, Catal. Lett. 12 (1992) 45–50, https://doi.org/10.1007/BF00767187.

[54] O.S. Owen, H.H. Kung, Effect of cation reducibility on oxidative dehydrogenation of butane on orthovanadates, J. Mol. Catal. 79 (1993) 265–284, https://doi.org/10.1016/0304-5102(93)85107-5.

[55] M.C. Kung, K.T. Nguyen, D. Patel, H.H. Kung, Selective Oxidative Dehydrogenation of Light Alkanes over Vanadate Catalysts, in: D.W. Blackburn (Ed.), Catalysis of Organic Reactions, CRC Press, 2020: pp. 289–300. doi: 10.1201/9781003066446-24.

[56] S. Sugiyama, T. Hashimoto, Y. Morishita, N. Shigemoto, H. Hayashi, Effects of calcium cations incorporated into magnesium vanadates on the redox behaviors and the catalytic activities for the oxidative dehydrogenation of propane, Appl. Catal. A 270 (2004) 253–260, https://doi.org/10.1016/j.apcata.2004.05.018.

[57] S. Sugiyama, T. Osaka, T. Hashimoto, K.I. Sotowa, Oxidative Dehydrogenation of Propane on Calcium Hydroxyapatites Partially Substituted with Vanadate, Catal. Lett. 103 (2005) 121–123, https://doi.org/10.1007/s10562-005-6513-7.

[58] C.T. Au, W.D. Zhang, H.L. Wan, Preparation and characterization of rare earth orthovanadates for propane oxidative dehydrogenation, Catal. Lett. 37 (1996) 241–246, https://doi.org/10.1007/BF00807761.

[59] R.X. Valenzuela, E.A. Mamedov, V.C. Corberan, Effect of different additives on the performance of V−Mg−O catalysts in the oxidative dehydrogenation of propane, React. Kinet. Catal. Lett. 55 (1995) 213–220, https://doi.org/10.1007/BF02075853.

[60] A. Dejoz, J.M. López Nieto, F. Márquez, M.I. Vázquez, The role of molybdenum in Mo-doped V-Mg–O catalysts during the oxidative dehydrogenation of n-butane, Appl. Catal. A 180 (1999) 83–94, https://doi.org/10.1016/S0926-860X(98)00332-9.

[61] R. Dula, K. Wcisło, J. Stoch, B. Grzybowska, E.M. Serwicka, F. Kooli, K. Bahranowski, A. Gaweł, Layered double hydroxide-derived vanadium catalysts for oxidative dehydrogenation of propane, Appl. Catal. A 230 (2002) 281–291, https://doi.org/10.1016/S0926-860X(02)00041-8.

[62] S. Sugiyama, T. Osaka, Y. Hirata, Y. Kondo, K. Nakagawa, K.-I. Sotowa, Redox nature of Fe-incorporated magnesium ortho-vanadate as a catalyst for the oxidative dehydrogenation of propane, J. Chem. Eng. Japan/JCEJ. 40 (2007) 1064–1071, https://doi.org/10.1252/jcej.07WE130.

[63] M. Jin, P. Lu, G.X. Yu, Z.M. Cheng, L.F. Chen, J.A. Wang, Effect of additives doping on catalytic properties of Mg3(VO4)2 catalysts in oxidative dehydrogenation of cyclohexane, Catal. Today. 212 (2013) 142–148, https://doi.org/10.1016/j.cattod.2012.09.019.

[64] E.A. Elkhalifa, H.B. Friedrich, Dehydrocyclization of n-octane over boron- and barium-doped V-Mg-O catalysts: influence of n-octane/oxygen ratios, Appl. Petrochem. Res. 7 (2017) 23–32, https://doi.org/10.1007/s13203-016-0174-x.

[65] V. Ermini, E. Finocchio, S. Sechi, G. Busca, S. Rossini, Propane oxydehydrogenation over alumina-supported vanadia doped with manganese and potassium, Appl. Catal. A 198 (2000) 67–79, https://doi.org/10.1016/S0926-860X(99)00499-8.

[66] Z. Liu, K. Sun, M. Wei, Z. Ma, Phosphorus-doped cerium vanadate nanorods with enhanced photocatalytic activity, J. Colloid Interface Sci. 531 (2018) 618–627, https://doi.org/10.1016/j.jcis.2018.07.077.

[67] D.L. Stern, J.N. Michaels, L. DeCaul, R.K. Grasselli, Oxydehydrogenation of n-butane over promoted Mg-V-oxide based catalysts, Appl. Catal. A 153 (1997) 21–30, https://doi.org/10.1016/S0926-860X(97)80115-9.

[68] L. Owens, H.H. Kung, The effect of loading of vanadia on silica in the oxidation of butane, J. Catal. 144 (1993) 202–213, https://doi.org/10.1006/jcat.1993.1324.

[69] A. Pantazidis, S.A. Bucholz, H.W. Zanthoff, Y. Schuurman, C. Mirodatos, A TAP reactor investigation of the oxidative dehydrogenation of propane over a V-Mg–O catalyst, Catal. Today. 40 (1998) 207–214, https://doi.org/10.1016/S0920-5861(98)00009-1.

[70] D. Creaser, B. Andersson, R.R. Hudgins, P.L. Silveston, Transient kinetic analysis of the oxidative dehydrogenation of propane, J. Catal. 182 (1999) 264–269, https://doi.org/10.1006/jcat.1998.2336.

[71] Y. Wang, P. Hu, J. Yang, Y.-A. Zhu, D. Chen, C-H bond activation in light alkanes: a theoretical perspective, Chem. Soc. Rev. 50 (2021) 4299–4358, https://doi.org/10.1039/d0cs01262a.

[72] O.O. James, S. Mandal, N. Alele, B. Chowdhury, S. Maity, Lower alkanes dehydrogenation: Strategies and reaction routes to corresponding alkenes, Fuel Process. Technol. 149 (2016) 239–255, https://doi.org/10.1016/j.fuproc.2016.04.016.

[73] M. Zboray, A.T. Bell, E. Iglesia, Role of C−H bond strength in the rate and selectivity of oxidative dehydrogenation of alkanes, J. Phys. Chem. C 113 (2009) 12380–12386, https://doi.org/10.1021/jp901595k.

[74] S. Zhang, H. Liu, Insights into the structural requirements for oxidative dehydrogenation of propane on crystalline Mg-V-O catalysts, Appl. Catal. A 568 (2018) 1–10, https://doi.org/10.1016/j.apcata.2018.09.019.

[75] P. Rybarczyk, H. Berndt, J. Radnik, M.M. Pohl, O. Buyevskaya, M. Baerns, A. Brückner, The structure of active sites in Me–V–O catalysts (Me = Mg, Zn, Pb) and its influence on the catalytic performance in the oxidative dehydrogenation (ODH) of propane, J. Catal. 202 (2001) 45–58, https://doi.org/10.1006/jcat.2001.3251.

[76] A. Guerrero-Ruiz, I. Rodriguez-Ramos, J.L.G. Fierro, V. Soenen, J.M. Herrmann, J.C. Volta, Nature Of Surface Sites In The Selective Oxide Hydrogenation Of Propane Over V-Mg-O Catalysts, in: New Developments in Selective Oxidation by Heterogeneous Catalysis, Elsevier, 1992, pp. 203–212. doi: 10.1016/S0167-2991(08)61672-9.

[77] V. Soenen, J.M. Herrmann, J.C. Volta, *In Situ* electrical characterization of magnesium vanadate reference phases (meta-MgV_2O_6, pyro-$Mg_2V_2O_7$, and ortho-$Mg_3V_2O_8$) used in oxidative dehydrogenation of propane to propene, J. Catal. 159 (1996) 410–417, https://doi.org/10.1006/jcat.1996.0104.

[78] Z.-Q. Wang, D. Wang, X.-Q. Gong, Strategies to improve the activity while maintaining the selectivity of oxidative coupling of methane at la2 o3: a density functional theory study, ACS Catal. 10 (2020) 586–594, https://doi.org/10.1021/acscatal.9b03066.

[79] S. Lim, J.-W. Choi, D.J. Suh, K.H. Song, H.C. Ham, J.-M. Ha, Combined experimental and density functional theory (DFT) studies on the catalyst design for the oxidative coupling of methane, J. Catal. 375 (2019) 478–492, https://doi.org/10.1016/j.jcat.2019.04.008.

[80] Q. Zhou, Z.-Q. Wang, Z. Li, J. Wang, M. Xu, S. Zou, J. Yang, Y. Pan, X.-Q. Gong, L. Xiao, J. Fan, $CH_3^{\bullet}$ -generating capability as a reactivity descriptor for metal oxides in oxidative coupling of methane, ACS Catal. (2021) 14651–14659, https://doi.org/10.1021/acscatal.1c03496.

[81] G. Kumar, S.L.J. Lau, M.D. Krcha, M.J. Janik, Correlation of methane activation and oxide catalyst reducibility and its implications for oxidative coupling, ACS Catal. 6 (2016) 1812–1821, https://doi.org/10.1021/acscatal.5b02657.

[82] P. Deshlahra, E. Iglesia, Reactivity and selectivity descriptors for the activation of C-H bonds in hydrocarbons and oxygenates on metal oxides, J. Phys. Chem. C 120 (2016) 16741–16760, https://doi.org/10.1021/acs.jpcc.6b04604.

[83] Y. Liu, L. Annamalai, P. Deshlahra, Effects of lattice O atom coordination and pore confinement on selectivity limitations for ethane oxidative dehydrogenation catalyzed by vanadium-oxo species, J. Phys. Chem. C 123 (2019) 28168–28191, https://doi.org/10.1021/acs.jpcc.9b07778.

[84] V. Fung, F. (Feng) Tao, D. Jiang, Trends of alkane activation on doped cobalt (II, III) oxide from first principles, ChemCatChem 10 (2018) 244–249, https://doi.org/10.1002/cctc.201700960.

[85] C. Tan, H. Liu, Y. Qin, L. Li, H. Wang, X. Zhu, Q. Ge, Correlation between the properties of surface lattice oxygen on NiO and its reactivity and selectivity towards the oxidative dehydrogenation of propane, ChemPhysChem (2022) e202200539.

[86] X. Rozanska, J. Sauer, Oxidative dehydrogenation of hydrocarbons by V3O7(+) compared to other vanadium oxide species, J. Phys. Chem. A 113 (2009) 11586–11594, https://doi.org/10.1021/jp9005235.

[87] A.D. Mayernick, M.J. Janik, Methane activation and oxygen vacancy formation over CeO_2 and Zr, Pd substituted CeO_2 surfaces, J. Phys. Chem. C 112 (2008) 14955–14964, https://doi.org/10.1021/jp805134s.

[88] M.D. Krcha, A.D. Mayernick, M.J. Janik, Periodic trends of oxygen vacancy formation and C-H bond activation over transition metal-doped CeO_2 (111) surfaces, J. Catal. 293 (2012) 103–115, https://doi.org/10.1016/j.jcat.2012.06.010.

[89] M.D. Krcha, M.J. Janik, Examination of oxygen vacancy formation in Mn-doped CeO_2 (111) using DFT+U and the hybrid functional HSE06, Langmuir 29 (2013) 10120–10131, https://doi.org/10.1021/la401747n.

[90] M.D. Krcha, M.J. Janik, Catalytic propane reforming mechanism over Zr-doped CeO_2 (111), Catal. Sci. Technol. 4 (2014) 3278, https://doi.org/10.1039/C4CY00619D.

[91] M.D. Krcha, M.J. Janik, Catalytic propane reforming mechanism over Mn-Doped CeO_2 (111), Surf. Sci. 640 (2015) 119–126, https://doi.org/10.1016/j.susc.2015.02.012.

[92] H.Y. Kim, H.M. Lee, R.G.S. Pala, V. Shapovalov, H. Metiu, CO Oxidation by Rutile TiO_2 (110) Doped with V, W, Cr, Mo, and Mn, J. Phys. Chem. C 112 (2008) 12398–12408, https://doi.org/10.1021/jp802296g.

[93] T.S. Kharlamova, K.L. Timofeev, M.A. Salaev, V.A. Svetlichnyi, O.V. Vodyankina, Monolayer $MgVO_x/Al_2O_3$ catalysts for propane oxidative dehydrogenation: Insights into a role of structural, redox, and acid-base properties in catalytic performance, Appl. Catal. A 598 (2020) 117574, https://doi.org/10.1016/j.apcata.2020.117574.

[94] L. Balderas-Tapia, I. Hernández-Pérez, P. Schacht, I.R. Córdova, G.G. Aguilar-Ríos, Influence of reducibility of vanadium–magnesium mixed oxides on the oxidative dehydrogenation of propane, Catal. Today 107–108 (2005) 371–376, https://doi.org/10.1016/j.cattod.2005.07.025.

[95] V.-K. Nguyen, J.-H. Park, C.-H. Shin, Characterization and activity of V_2O_5/CeO_2-MgO catalyst in the dehydrogenation of ethylbenzene to styrene, Korean J. Chem. Eng. 31 (2014) 582–586, https://doi.org/10.1007/s11814-013-0265-7.

[96] A. Corma, J.M. Lopez-Nieto, N. Paredes, Influence of the Preparation Methods of V-Mg-O Catalysts on Their Catalytic Properties for the Oxidative Dehydrogenation of Propane, J. Catal. 144 (1993) 425–438, https://doi.org/10.1006/jcat.1993.1343.

[97] J. Sauer, J. Dobler, Structure and reactivity of V(2)O(5): bulk solid, nanosized clusters, species supported on silica and alumina, cluster cations and anions, Dalton Trans. (2004) 3116–3121, https://doi.org/10.1039/b402873b.

[98] T.K. Todorova, M.V. Ganduglia-Pirovano, J. Sauer, Vanadium oxides on aluminum oxide supports. 1. Surface termination and reducibility of vanadia films on alpha-Al2O3(0001), J. Phys. Chem. b. 109 (2005) 23523–23531, https://doi.org/10.1021/jp053899l.

[99] M.V. Ganduglia-Pirovano, C. Popa, J. Sauer, H. Abbott, A. Uhl, M. Baron, D. Stacchiola, O. Bondarchuk, S. Shaikhutdinov, H.-J. Freund, Role of ceria in oxidative dehydrogenation on supported vanadia catalysts, J. Am. Chem. Soc. 132 (2010) 2345–2349, https://doi.org/10.1021/ja910574h.

[100] C. Penschke, J. Paier, J. Sauer, Oligomeric vanadium oxide species supported on the ceo_2 (111) surface: structure and reactivity studied by density functional theory, J. Phys. Chem. c. 117 (2013) 5274–5285, https://doi.org/10.1021/jp400520j.

[101] V. Fung, F. Polo-Garzon, Z. Wu, D. Jiang, Exploring perovskites for methane activation from first principles, Catal. Sci. Technol. (2018), https://doi.org/10.1039/C7CY01791J.

[102] L. Foppa, F. Rüther, M. Geske, G. Koch, F. Girgsdies, P. Kube, S.J. Carey, M. Hävecker, O. Timpe, A.V. Tarasov, M. Scheffler, F. Rosowski, R. Schlögl, A. Trunschke, Data-centric heterogeneous catalysis: identifying rules and materials genes of alkane selective oxidation, J. Am. Chem. Soc. 145 (2023) 3427–3442, https://doi.org/10.1021/jacs.2c11117.

[103] G. Kresse, J. Hafner, *Ab initio* molecular dynamics for liquid metals, Phys. Rev. B 47 (1993) 558–561, https://doi.org/10.1103/PhysRevB.47.558.

[104] G. Kresse, J. Hafner, *Ab initio* molecular-dynamics simulation of the liquid-metal–amorphous-semiconductor transition in germanium, Phys. Rev. B 49 (1994) 14251–14269, https://doi.org/10.1103/PhysRevB.49.14251.

[105] G. Kresse, J. Furthmüller, Efficient iterative schemes for *ab initio* total-energy calculations using a plane-wave basis set, Phys. Rev. B 54 (1996) 11169–11186, https://doi.org/10.1103/PhysRevB.54.11169.

[106] G. Kresse, J. Furthmüller, Efficiency of ab-initio total energy calculations for metals and semiconductors using a plane-wave basis set, Comp. Mater. Sci. 6 (1996) 15–50, https://doi.org/10.1016/0927-0256(96)00008-0.

[107] P. Kravchenko, C. Plaisance, D. Hibbitts, A new computational interface for catalysis, Published as pre-print on doi: 10.26434/chemrxiv.8040737.v4 (2019). doi: 10.26434/chemrxiv.8040737.v3.

[108] J.P. Perdew, K. Burke, M. Ernzerhof, Generalized gradient approximation made simple, Phys. Rev. Lett. 77 (1996) 3865–3868, https://doi.org/10.1103/PhysRevLett.77.3865.

[109] Y. Zhang, W. Yang, Comment on "Generalized Gradient Approximation Made Simple", Phys. Rev. Lett. 80 (1998) 890, https://doi.org/10.1103/PhysRevLett.80.890.

[110] E. Sargeant, F. Illas, P. Rodríguez, F. Calle-Vallejo, Importance of the gas-phase error correction for O_2 when using DFT to model the oxygen reduction and evolution reactions, J. Electroanal. Chem. 896 (2021) 115178, https://doi.org/10.1016/j.jelechem.2021.115178.

[111] M.O. Almeida, M.J. Kolb, M.R.V. Lanza, F. Illas, F. Calle-Vallejo, Gas-phase errors affect dft-based electrocatalysis models of oxygen reduction to hydrogen peroxide, ChemElectroChem 9 (2022), https://doi.org/10.1002/celc.202200210.

[112] L. Wang, T. Maxisch, G. Ceder, Oxidation energies of transition metal oxides within the GGA+U framework, Phys. Rev. B 73 (2006) 195107, https://doi.org/10.1103/PhysRevB.73.195107.

[113] V.I. Anisimov, O. Gunnarsson, Density-functional calculation of effective Coulomb interactions in metals, Phys. Rev., B Condens. Matter. 43 (1991) 7570–7574, https://doi.org/10.1103/physrevb.43.7570.

[114] J.F. Herbst, R.E. Watson, J.W. Wilkins, Relativistic calculations of 4f excitation energies in the rare-earth metals: further results, Phys. Rev. B 17 (1978) 3089–3098, https://doi.org/10.1103/PhysRevB.17.3089.

[115] S.A. Tolba, K.M. Gameel, B.A. Ali, H.A. Almossalami, N.K. Allam, The DFT+U: approaches, accuracy, and applications, in: G. Yang (Ed.), Density Functional Calculations - Recent Progresses of Theory and Application, InTech, 2018. doi: 10.5772/intechopen.72020.

[116] H.H. Kristoffersen, H. Metiu, Reconstruction of Low-Index α-V_2O_5 Surfaces, J. Phys. Chem. c. 119 (2015) 10500–10506, https://doi.org/10.1021/acs.jpcc.5b02383.

[117] R. Defrance, B. Sklénard, M. Guillaumont, J. Li, M. Freyss, Ab initio study of electron mobility in VO via polaron hopping, Solid State Electron. 198 (2022) 108455, https://doi.org/10.1016/j.sse.2022.108455.

[118] T. Das, S. Tosoni, G. Pacchioni, Structural and electronic properties of bulk and ultrathin layers of V_2O_5 and MoO_3, Comp. Mater. Sci. 163 (2019) 230–240, https://doi.org/10.1016/j.commatsci.2019.03.027.

[119] W. Song, T. Liu, L. Yang, J. Jiang, Thermodynamics of native defects in V_2O_5 crystal: a first-principles method, Comp. Mater. Sci. 220 (2023) 112071, https://doi.org/10.1016/j.commatsci.2023.112071.

[120] D. Koch, S. Manzhos, Interstitial versus substitutional metal insertion in V_2O_5 as post-lithium ion battery cathode: a comparative GGA/GGA+U study with localized bases, MRS Commun. 10 (2020) 259–264, https://doi.org/10.1557/mrc.2020.36.

[121] V.I. Anisimov, J. Zaanen, O.K. Andersen, Band theory and Mott insulators: Hubbard *U* instead of Stoner *I*, Phys. Rev. B 44 (1991) 943–954, https://doi.org/10.1103/PhysRevB.44.943.

[122] Y. Liu, Q. Hu, D. Ma, X. Liu, Z. You, G. Qiu, X. Lv, Periodic DFT study on the adsorption and deoxygenation process of NH_3 on V_2O_5 (001) surface, JOM 74 (2022) 1870–1877, https://doi.org/10.1007/s11837-022-05256-6.

[123] V.A. Ranea, P.L. Dammig Quiña, N.M. Yalet, General adsorption model for H_2S, H_2Se, H_2Te, NH_3, PH_3, AsH_3 and SbH_3 on the V_2O_5(001) surface including the van der Waals interaction, Chem. Phys. Lett. 720 (2019) 58–63, https://doi.org/10.1016/j.cplett.2019.02.013.

[124] N.M. Yalet, V.A. Ranea, A DFT+U study on the adsorption of CO, H_2S, PH_3, CO_2 and SO_2 on the V_2O_5(001) surface with atomic Rh adsorbed, Surf. Sci. 718 (2022) 122014, https://doi.org/10.1016/j.susc.2021.122014.

[125] A.D. Costa, C. Mathieu, Y. Barbaux, H. Poelman, G. Dalmai-Vennik, L. Fiermans, Observation of the V_2O_5(001) surface using ambient atomic force microscopy, Surf. Sci. 370 (1997) 339–344, https://doi.org/10.1016/S0039-6028(96)00956-9.

[126] K. Tarama, S. Yoshida, S. Ishida, H. Kakioka, Spectroscopic studies of catalysis by vanadium pentoxide, Bull. Chem. Soc. Jpn. 41 (1968) 2840–2845, https://doi.org/10.1246/bcsj.41.2840.

[127] R. Ramirez, B. Casal, L. Utrera, E. Ruiz-Hitzky, Oxygen reactivity in vanadium pentoxide: electronic structure and infrared spectroscopy studies, J. Phys. Chem. 94 (1990) 8960–8965, https://doi.org/10.1021/j100389a021.

[128] R.A. Goschke, K. Vey, M. Maier, U. Walter, E. Goering, M. Klemm, S. Horn, Tip induced changes of atomic scale images of the vanadium pentoxide surface, Surf. Sci. 348 (1996) 305–310, https://doi.org/10.1016/0039-6028(95)00998-1.

[129] A. Chakrabarti, K. Hermann, R. Druzinic, M. Witko, F. Wagner, M. Petersen, Geometric and electronic structure of vanadium pentoxide: a density functional bulk and surface study, Phys. Rev. B 59 (1999) 10583–10590, https://doi.org/10.1103/PhysRevB.59.10583.

[130] E. Londero, E. Schröder, Vanadium pentoxide (V_2O_5): A van der Waals density functional study, Comput. Phys. Commun. 182 (2011) 1805–1809, https://doi.org/10.1016/j.cpc.2010.12.036.

[131] X. Yin, A. Fahmi, A. Endou, R. Miura, I. Gunji, R. Yamauchi, M. Kubo, A. Chatterjee, A. Miyamoto, Periodic density functional study on V_2O_5 bulk and (001) surface, Appl. Surf. Sci. 130–132 (1998) 539–544, https://doi.org/10.1016/S0169-4332(98)00111-1.

[132] E. Londero, E. Schröder, Role of van der Waals bonding in the layered oxide: First-principles density-functional calculations, Phys. Rev. B 82 (2010) 054116, https://doi.org/10.1103/PhysRevB.82.054116.

[133] A. Burrows, C.J. Kiely, J. Perregaard, P.E. Hojlund-Nielsen, G. Vorbeck, J.J. Calvino, C. Lopez-Cartes, Structural characterisation of a VMgO catalyst used in the oxidative dehydrogenation of propane, Springer Science and Business Media LLC, 1999. doi: 10.1023/a:1019035229609.

[134] T. Zhang, Q. Gui, Y. Zhou, J. Yang, H. Zeng, Q. Peng, Q. Ye, D. Yang, Y. Li, First principles investigation of electronic structure, elasticity, thermodynamic properties and lattice thermal conductivity of $Mg_2V_2O_7$, Comput. Theor. Chem. 1220 (2023) 113988, https://doi.org/10.1016/j.comptc.2022.113988.

[135] U.G. Nielsen, H.J. Jakobsen, J. Skibsted, P. Norby, Crystal structure of α-$Mg_2V_2O_7$ from synchrotron X-ray powder diffraction and characterization by ^{51}V MAS NMR spectroscopy, J. Chem. Soc., Dalton Trans. (2001) 3214–3218, https://doi.org/10.1039/b104454k.

[136] G. Pei, C. Pan, D. Zhong, J. Xiang, X. Lv, Crystal structure, phase transitions, and thermodynamic properties of magnesium metavanadate (MgV_2O_6), J. Magnesium Alloys (2022), https://doi.org/10.1016/j.jma.2022.05.011.

[137] M.A. Rahman, M.A.R. Sarker, Synthesis, characterization and physical properties of high quality MgV_2O_6 crystals by solid-state reaction and ab-initio methods, J Alloys Compd. 797 (2019) 630–639, https://doi.org/10.1016/j.jallcom.2019.05.081.

[138] M.A. Boda, C. Chen, X. He, L. Wang, Z. Yi, High photostrictive efficiency of $Mg_3V_2O_8$ ceramics under visible light illumination, J. Am. Ceram. Soc. 106 (2023) 3584–3593, https://doi.org/10.1111/jace.19042.

[139] G. Pei, J. Xiang, L. Yang, X. Lv, Thermodynamic properties of magnesium orthovanadate Mg3(VO4)2 at high temperatures (298.15–1473 K), Calphad 74 (2021) 102295, https://doi.org/10.1016/j.calphad.2021.102295.

[140] G. Busca, G. Ricchiardi, D.S.H. Sam, J.-C. Volta, Spectroscopic characterization of magnesium vanadate catalysts. Part 1. —vibrational characterization of Mg3(VO4)2, Mg2V2O7 and MgV2O6 powders, J. Chem. Soc., Faraday Trans. 90 (1994) 1161–1170, https://doi.org/10.1039/FT9949001161.

[141] X.T. Gao, P. Ruiz, Q. Xin, X.X. Guo, B. Delmon, Effect of coexistence of magnesium vanadate phases in the selective oxidation of propane to propene, J. Catal. 148 (1994) 56–67, https://doi.org/10.1006/jcat.1994.1185.

[142] S. Zhang, H. Liu, Oxidative dehydrogenation of propane over Mg-V-O oxides supported on MgO-coated silica: structural evolution and catalytic consequence, Appl. Catal. A 573 (2019) 41–48, https://doi.org/10.1016/j.apcata.2019.01.012.

[143] G. Busca, Differentiation of mono-oxo and polyoxo and of monomeric and polymeric vanadate, molybdate and tungstate species in metal oxide catalysts by IR and Raman spectroscopy, J. Raman Spectrosc. 33 (2002) 348–358, https://doi.org/10.1002/jrs.867.

[144] X. Gao, P. Ruiz, Q. Xin, X. Guo, B. Delmon, Preparation and characterization of three pure magnesium vanadate phases as catalysts for selective oxidation of propane to propene, Catal. Lett. 23 (1994) 321–337, https://doi.org/10.1007/BF00811367.

[145] H. Jónsson, G. Mills, K.W. Jacobsen, Nudged elastic band method for finding minimum energy paths of transitions, in: B.J. Berne, G. Ciccotti, D.F. Coker (Eds.), Classical and Quantum Dynamics in Condensed Phase Simulations, World Scientific, 1998, pp. 385–404, https://doi.org/10.1142/9789812839664_0016.

[146] G. Henkelman, B.P. Uberuaga, H. Jónsson, A climbing image nudged elastic band method for finding saddle points and minimum energy paths, J. Chem. Phys. 113 (2000) 9901–9904, https://doi.org/10.1063/1.1329672.

[147] G. Henkelman, H. Jónsson, Improved tangent estimate in the nudged elastic band method for finding minimum energy paths and saddle points, J. Chem. Phys. 113 (2000) 9978–9985, https://doi.org/10.1063/1.1323224.

[148] G. Henkelman, H. Jónsson, A dimer method for finding saddle points on high dimensional potential surfaces using only first derivatives, J. Chem. Phys. 111 (1999) 7010–7022, https://doi.org/10.1063/1.480097.

[149] X. Rozanska, R. Fortrie, J. Sauer, Size-dependent catalytic activity of supported vanadium oxide species: oxidative dehydrogenation of propane, J. Am. Chem. Soc. 136 (2014) 7751–7761, https://doi.org/10.1021/ja503130z.

[150] C.P. Plaisance, R.A. van Santen, K. Reuter, Constrained-orbital density functional theory. computational method and applications to surface chemical processes, J. Chem. Theory Comput. 13 (2017) 3561–3574, https://doi.org/10.1021/acs.jctc.7b00362.

[151] B. Kaduk, T. Kowalczyk, T. Van Voorhis, Constrained density functional theory, Chem. Rev. 112 (2012) 321–370, https://doi.org/10.1021/cr200148b.

[152] Y. Chen, G. Yang, Z. Zhang, X. Yang, W. Hou, J.-J. Zhu, Polyaniline-intercalated layered vanadium oxide nanocomposites–one-pot hydrothermal synthesis and application in lithium battery, Nanoscale 2 (2010) 2131–2138, https://doi.org/10.1039/c0nr00246a.

[153] V. Nicolosi, M. Chhowalla, M.G. Kanatzidis, M.S. Strano, J.N. Coleman, Liquid exfoliation of layered materials, Science 340 (2013) 1226419, https://doi.org/10.1126/science.1226419.

[154] X. Rui, Z. Lu, H. Yu, D. Yang, H.H. Hng, T.M. Lim, Q. Yan, Ultrathin V_2O_5 nanosheet cathodes: realizing ultrafast reversible lithium storage, Nanoscale 5 (2013) 556–560, https://doi.org/10.1039/c2nr33422d.

[155] S. Guimond, J.M. Sturm, D. Göbke, Y. Romanyshyn, M. Naschitzki, H. Kuhlenbeck, H.-J. Freund, Well-ordered V_2O_5 (001) thin films on Au(111): growth and thermal stability, J. Phys. Chem. C 112 (2008) 11835–11846, https://doi.org/10.1021/jp8011156.

[156] Q.-H. Wu, A. Thissen, W. Jaegermann, M. Liu, Photoelectron spectroscopy study of oxygen vacancy on vanadium oxides surface, Appl. Surf. Sci. 236 (2004) 473–478, https://doi.org/10.1016/j.apsusc.2004.05.112.

[157] Z. Zhang, V.E. Henrich, Surface electronic structure of V_2O_5(001): defect states and chemisorption, Surf. Sci. 321 (1994) 133–144, https://doi.org/10.1016/0039-6028(94)90034-5.

[158] M.V. Ganduglia-Pirovano, J. Sauer, Stability of reduced V_2O_5(001) surfaces, Phys. Rev. b. 70 (2004) 045422, https://doi.org/10.1103/PhysRevB.70.045422.

[159] A.S. Negreira, S. Aboud, J. Wilcox, Surface reactivity of V_2O_5(001): Effects of vacancies, protonation, hydroxylation, and chlorination, Phys. Rev. B 83 (2011) 045423, https://doi.org/10.1103/PhysRevB.83.045423.

[160] X. Gao, I.E. Wachs, Investigation of surface structures of supported vanadium oxide catalysts by uv−vis−nir diffuse reflectance spectroscopy, J. Phys. Chem. B 104 (2000) 1261–1268, https://doi.org/10.1021/jp992867t.

[161] A.R. Derk, B. Li, S. Sharma, G.M. Moore, E.W. McFarland, H. Metiu, Methane oxidation by lanthanum oxide doped with Cu, Zn, Mg, Fe, Nb, Ti, Zr, or Ta: the connection between the activation energy and the energy of oxygen-vacancy formation, Catal. Lett. 143 (2013) 406–410, https://doi.org/10.1007/s10562-013-0985-7.

[162] A. Vojvodic, F. Calle-Vallejo, W. Guo, S. Wang, A. Toftelund, F. Studt, J. I. Martínez, J. Shen, I.C. Man, J. Rossmeisl, T. Bligaard, J.K. Noørskov, F. Abild-Pedersen, On the behavior of Brønsted-Evans-Polanyi relations for transition metal oxides, J. Chem. Phys. 134 (2011) 244509, https://doi.org/10.1063/1.3602323.

[163] C.P. Plaisance, K. Reuter, R.A. van Santen, Quantum chemistry of the oxygen evolution reaction on cobalt(II, III) oxide - implications for designing the optimal catalyst, Faraday Discuss. 188 (2016) 199–226, https://doi.org/10.1039/c5fd00213c.